ROYAL SOCIETY
OF CHEMISTRY

REVIEW

Check for updates

Inorganic sulfide solid electrolytes for all-solid-state lithium secondary batteries

Peng-Jie Lian,[a] Bo-Sheng Zhao,[a] Lian-Qi Zhang,*[b] Ning Xu,[c] Meng-Tao Wu[c] and Xue-Ping Gao [ID] *[a]

Liquid organic electrolytes are mostly used in commercial lithium-ion batteries, due to their advantages of high conductivity and excellent wetting of the electrode interface. However, liquid organic electrolytes are flammable and volatile, causing safety issues of commercial lithium-ion batteries in electric vehicles. Recently, all-solid-state lithium secondary batteries have attracted great attention owing to their high safety and increased energy density, and are considered the most promising next generation energy storage systems. The most essential components are solid electrolytes for all-solid-state lithium batteries. Among various inorganic solid electrolytes, sulfide solid electrolytes have received widespread attention because of their high ionic conductivity and good mechanical properties. Herein, we summarize the development of several typical sulfide solid electrolytes and the problems to be addressed in emerging all-solid-state lithium batteries. Finally, the future development directions of sulfide electrolytes and all-solid-state lithium batteries are briefly discussed.

1 Introduction

With the rapid development of new energy technologies, the demand for secondary battery systems with high energy density and high safety has become increasingly urgent. According to a worldwide technical goal, the energy density of secondary batteries needs to reach 500 W h kg^{-1} in 2030. However, current lithium-ion batteries (LIBs) can hardly achieve this target.[1-3] Commercial LIBs mostly employ liquid organic electrolytes, which show flammable and volatile features compared to the solid electrolytes (SEs) with high safety.[4,5] Compared to traditional LIBs with liquid electrolytes, all-solid-state lithium secondary batteries using SEs theoretically have the following features: (1) higher safety due to the mechanical prevention of leaking and burning of SEs; (2) bi-function of SEs as separators and electrolytes in all-solid-state batteries; (3) better mechanical strength for ensuring long-term operation, compared with traditional polymer separators; (4) fewer side reactions between SEs and electrodes; (5) wider electrochemical window of SEs, as compared with liquid organic electrolytes; (6) high lithium ion migration number close to 1 in SEs. However, there are still great challenges for all-solid-state lithium secondary batteries compared to LIBs with liquid electrolytes: (1) poor wettability for solid electrolytes, resulting in poor contact between SEs and

active materials compared to liquid electrolytes; (2) unstable rigid interface between SEs and active materials due to the volume expansion and contraction of active materials during cycling, which can damage or terminate the battery; (3) unsuccessful commercialization SEs for all-solid-state batteries based on considerations of high conductivity, high stability and low cost.

SEs can be classified into two main groups: inorganic solid electrolytes and polymer solid electrolytes. Polymer solid electrolytes with good mechanical properties are helpful in improving the battery safety performance during production and operation. However, polymer solid electrolytes are still unsatisfactory, due to their low conductivity, narrow electrochemical window, and poor stability at elevated temperatures.[6-8] The inorganic solid electrolytes, also known as lithium fast ion conductors, can be mainly classified into two types: oxide solid electrolytes (hereinafter referred to as O-SEs) and sulfide solid electrolytes (hereinafter referred to as S-SEs). There are many types of O-SEs: natrium superionic conductors (NASICON), perovskites, garnets, γ-Li$_3$PO$_4$, and some amorphous oxides, including Li$_2$O–MO$_x$ (M = Si, B, and P) and LiPON-related materials.[9-13] The O-SEs have good electrochemical stability and thermal stability, but relatively low conductivity (10^{-7} to 10^{-4} S cm^{-1} at room temperature) and rigid mechanical property, limiting their commercial application in battery systems.[14-16] The S-SEs are mainly composed of Li$_2$S and sulfides (such as SiS$_2$, P$_2$S$_5$, and GeS$_2$). Compared with O-SEs, the electronegativity of S^{2-} in S-SEs is less than that of O^{2-}, so the binding of lithium ions is weak and more free lithium ions migrate inside S-SEs. In addition, the radius of S^{2-}

[a]Institute of New Energy Material Chemistry, School of Materials Science and Engineering, Nankai University, Tianjin 300350, China. E-mail: xpgao@nankai.edu.cn; Fax: +86-22-23500876; Tel: +86-22-23500876

[b]School of Materials Science and Engineering, Tianjin University of Technology, Tianjin 300384, China. E-mail: lianqizhang@126.com

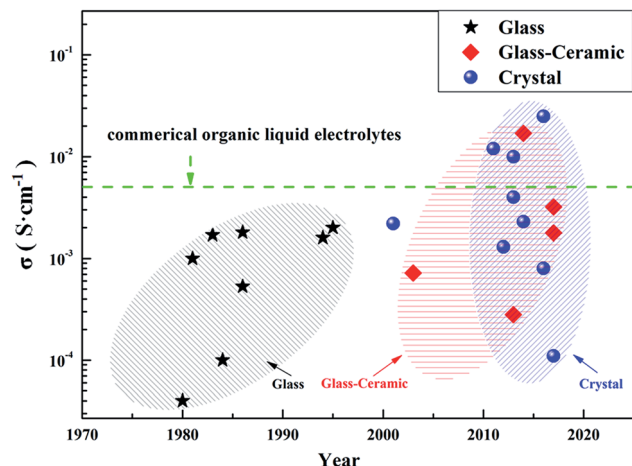*[c]Tianjin Bamo Tech Co., Ltd., Tianjin 300384, China*

Fig. 1 A graph of lithium ion conductivities of typical SEs.

is larger than that of O^{2-}, which is favourable for forming a large transmission channel of lithium ions. Therefore, S-SEs usually have higher lithium ion conductivity (10^{-5} to

10^{-2} S cm^{-1} at room temperature, Fig. 1) compared with O-SEs. Furthermore, S-SEs have better ductility than O-SEs, which is favourable for good contact between the electrode materials and S-SEs by simple cold pressing, as well as convenient for the manufacture of bulk all-solid-state batteries.[17,18] In this review, we summarize the development, intrinsic features, and applications of S-SEs in all-solid-state lithium secondary batteries. The emerging challenges and trends in all-solid-state lithium secondary batteries are also discussed.

2 Sulfide solid electrolytes

2.1 Lithium ion transport mechanism of S-SEs

S-SEs initially originated from Pradel's research on Li_2S–SiS_2 in 1986.[19] There are three ways of sulfur accumulation in SEs: body-centred cubic (BCC) stacking, face-centred cubic (FCC) stacking, and hexagonal close packing (HCP). In BCC stacking (for example, $Li_7P_3S_{11}$ and $Li_{10}GeP_2S_{12}$), Li-ions migrate along the path connecting the two coplanar tetrahedral sites (T_1 and T_2, Fig. 2a) with a very low barrier of 0.15 eV, called the T–T path.
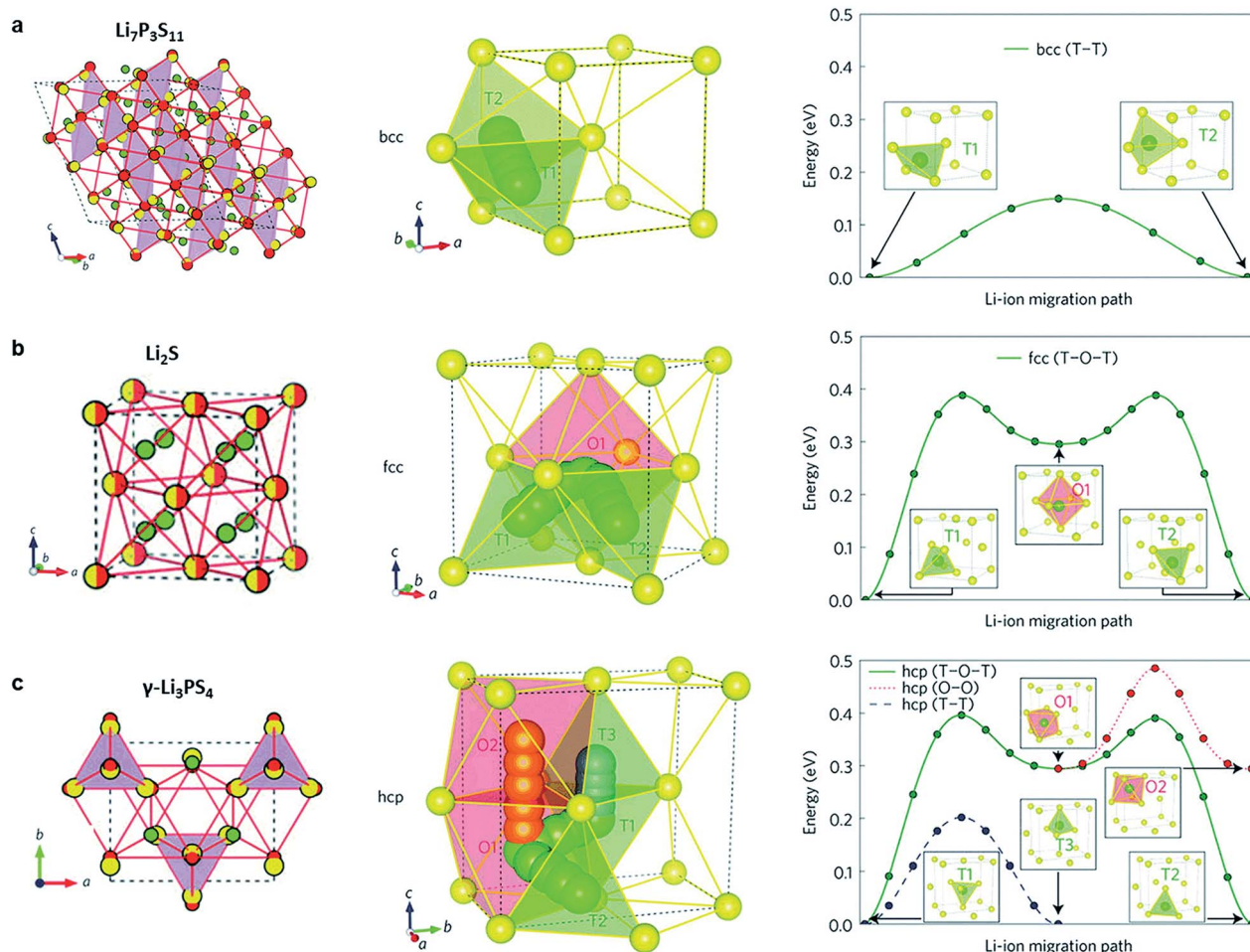

Fig. 2 (a–c) Crystal structures of the Li-ion conductors (a) $Li_7P_3S_{11}$, (b) Li_2S and (c) γ-Li_3PS_4. The Li ions, partially occupied Li$^+$ sites, S^{2-} anion, and PS$_4$ tetrahedral and GeS$_4$ tetrahedral sites (partially occupied in $Li_{10}GeP_2S_{12}$) are coloured green, green–white, yellow, purple and blue, respectively. In both $Li_{10}GeP_2S_{12}$ and $Li_7P_3S_{11}$, the sulfur anion sublattice can be closely mapped to a bcc framework (red circles connected by red lines). In Li_2S, the anion sublattice is an exact fcc matrix (yellow–red circles). The anion sublattices in γ-Li_3PS_4 and Li_4GeS_4 closely match to a hcp framework. Reprinted with permission.[15] Copyright© 2015, Springer Nature.

In FCC stacking (like Li_2S), Li-ions move from a tetrahedral site (T_1) to another tetrahedral site (T_2) through an intermediate octahedral site (O_1), which is called the T–O–T path, with a barrier of 0.39 eV (Fig. 2b). The T–O–T path can also be found in the a–b plane of the HCP lattice (T_1 to T_2 through O_1 in Fig. 2c) with almost the same activation barrier (0.40 eV). The migration of Li-ions along the c-axis in the HCP lattice is the T–T path through two face-sharing tetrahedral sites (T_1 and T_3, Fig. 2c) with a low barrier of 0.20 eV. Li-ions can also migrate across the path connecting two coplanar octahedral sites (O_1 and O_2, 0.19 eV, Fig. 2c) along the c-axis. However, the O–O path needs additional activation energy due to the instability of octahedral positions. Therefore, migration of Li-ions in the HCP lattice is likely to occur by an alternation of T–T and T–O–T paths. Therefore, the activation barrier of the lithium ion migration pathway in the body-centered-cubic anion framework is lower than that of other close-packed frameworks,[15] which is beneficial to achieve high ionic conductivity.

2.2 Crystalline state of S-SEs

According to their crystalline state, S-SEs can be divided into three categories: glass, glass-ceramic and crystal. Glassy electrolytes have attracted much attention due to their isotropic ion conduction, zero grain boundary resistance and low cost.[20] The ionic conductivity of glassy electrolytes can reach about 10^{-4} S cm^{-1} at room temperature.[21–24] Meanwhile, the glass-ceramic electrolytes obtained by crystallization from glassy electrolytes have higher conductivity, about 10^{-3} S cm^{-1} (even up to 10^{-2} S cm^{-1}), at room temperature.[25–29] This is because the glassy electrolyte softens and reduces the grain boundary resistance during the crystallization process. In addition, the precipitation of partial crystallites also helps improve the lithium ion conductivity. The crystal electrolytes will be mentioned in the next section.

There are three main methods for preparing S-SEs: melt quenching, mechanical milling, and wet chemistry. Table 1 shows a comparison of the three preparation methods. Considering feasibility and safety, most S-SEs are prepared by mechanical milling. This work mainly classifies the electrolytes based on their crystalline structure. According to their structures, S-SEs can be divided into the following two categories: thio-lithium super ion conductors (thio-LiSICONs) and argyrodite type.

2.2.1 Thio-LiSICONs. Thio-LiSICONs were first discovered by replacing O^{2-} with S^{2-} in LiSICONs.[30] The thio-LiSICONs with the general formula of $Li_{4-x}Ge_{1-x}P_xS_4$ exhibit the highest

Table 1 Advantages and disadvantages of the three methods for preparing S-SEs

Method	Advantage	Disadvantage
Melt quenching	Low equipment requirements	High temperature
	Easy to prepare bulk materials	Unsafe
	Suitable for preparing glass, glass-ceramic and crystal SEs	Complicated operation
Mechanical milling	Simple operation	Long working hours
	High safety	
	Easy to prepare powder materials	
	Suitable for preparing glass, glass-ceramic and crystal SEs	
Wet chemistry	Controllable morphology	Residual organic waste
	Easy to prepare powder materials	Strict preparation conditions
	Suitable for crystal SEs	

Table 2 Characteristic parameters of typical solid-state electrolytes

Composition	State	Ionic conductivity (S cm^{-1})	Activation energy (eV)	Ref.
$50Li_2S$–$50GeS_2$	Glass	4×10^{-5}	0.51	31
$60Li_2S$–$40SiS_2$	Glass	5.3×10^{-4}	0.33	19
$67Li_2S$–$33P_2S_5$	Glass	10^{-4}	0.36	32
$Li_7P_3S_{11}$	Glass-ceramic	3.2×10^{-3}	0.125	26
$Li_7P_3S_{11}$	Glass-ceramic	1.7×10^{-2}	0.18	21
Li_3PS_4	Glass-ceramic	2.8×10^{-4}	0.356	33 and 34
$78Li_2S$–$22P_2S_5$	Glass-ceramic	1.78×10^{-3}	0.31	35
$80Li_2S$–$20P_2S_5$	Glass-ceramic	7.2×10^{-4}	0.25	33
$Li_7Ge_3PS_{12}$	Crystal	1.1×10^{-4}	0.26	36
$Li_{3.25}Ge_{0.25}P_{0.75}S_4$	Crystal	2.2×10^{-3}	0.207	30
$Li_{9.54}Si_{1.74}P_{1.44}S_{11.7}Cl_{0.3}$	Crystal	2.5×10^{-2}	0.238	37
$Li_{10}GeP_2S_{12}$	Crystal	1.2×10^{-2}	0.21	38
$Li_{10}SnP_2S_{12}$	Crystal	4×10^{-3}	0.87	39
$Li_{10}SiP_2S_{12}$	Crystal	2.3×10^{-3}	0.20	40
$Li_{11}AlP_2S_{12}$	Crystal	8×10^{-4}	0.263	41
Li_6PS_5Cl	Crystal	1.3×10^{-3}	0.33	42
Li_6PS_5Br	Crystal	10^{-2}	0.20	43

20542 | J. Mater. Chem. A, 2019, 7, 20540–20557

This journal is © The Royal Society of Chemistry 2019

conductivity of 2.2×10^{-3} S cm^{-1}. The structure of most S-SEs is similar to the structure of Li$_{4-x}$Ge$_{1-x}$P$_x$S$_4$. Table 2 shows the characteristic parameters of typical S-SEs. According to the number of components, thio-LiSICONs can be mainly divided into binary systems of Li$_2$S–MS$_n$ (M = P, Si and B) and ternary systems of Li$_2$S–P$_2$S$_5$–MeS$_n$ (Me = Si, Ge and Sn).

2.2.1.1 Binary systems of Li$_2$S–MS$_n$. Li$_2$S–B$_2$S$_3$ and Li$_2$S–SiS$_2$ were reported as the earlier binary systems of Li$_2$S–MS$_n$. However, their ion conductivity is still unsatisfactory, although the conductivity can be improved to a certain extent by doping Li$_x$MO$_y$ (M = Si, Ge, P).[44] As the optimized binary system of Li$_2$S–MS$_n$, the Li$_2$S–P$_2$S$_5$ system has good physical and chemical properties and is widely used in all-solid-state batteries. In particular, Li$_2$S–P$_2$S$_5$ has a high ionic conductivity of 0.1 to 1×10^{-3} S cm^{-1} at room temperature[25–29] and a wide electrochemical window.

There are two typical compounds with high ionic conductivity in the binary system of Li$_2$S–P$_2$S$_5$: Li$_3$PS$_4$ (75% Li$_2$S–25% P$_2$S$_5$ molar ratio) and Li$_7$P$_3$S$_{11}$ (70% Li$_2$S–30% P$_2$S$_5$ molar ratio). Li$_3$PS$_4$ was first discovered in 1984 (ref. 45) and is considered the most stable compound in the binary system of Li$_2$S–P$_2$S$_5$.[46] Usually, Li$_3$PS$_4$ exists as γ-Li$_3$PS$_4$ with a conductivity of 3×10^{-7} S cm^{-1} at room temperature. When heated to 195 °C, γ-Li$_3$PS$_4$ is converted to β-Li$_3$PS$_4$ with a conductivity of 9×10^{-7} S cm^{-1}.[47] The crystalline structure of β-Li$_3$PS$_4$ is shown in Fig. 3a, where the PS$_4$ and LiS$_4$ tetrahedra are dominant. There have been many effective attempts for improving the conductivity of β-Li$_3$PS$_4$ in the past. After preparation by mechanical ball milling and subsequent heat treatment at 230 °C, Li$_3$PS$_4$ presents a high conductivity of 2.8×10^{-4} S cm^{-1} at room temperature.[33] A special β-Li$_3$PS$_4$ with nanopores (about 100 nm), prepared by wet chemistry, shows a conductivity of 1.6×10^{-4} S cm^{-1} at room temperature, which is nearly 3 orders of magnitude higher than that of crystalline Li$_3$PS$_4$. Meanwhile, the nanoporous Li$_3$PS$_4$ exhibits good compatibility with lithium and has a wide electrochemical window of 5 V.[34] A plate-like Li$_3$PS$_4$ (about 3 μm in length, 500 nm in width, and 100–200 nm in thickness), prepared by liquid-phase shaking, presents a conductivity as high as 2.0×10^{-4} S cm^{-1} at room temperature.[48]

In general, Li$_7$P$_3$S$_{11}$ is obtained in the 70% Li$_2$S–30% P$_2$S$_5$ composition and is an extremely important member of the binary system due to its very high ionic conductivity (up to 1.7×10^{-2} S cm^{-1} at RT).[21,49] Some types of fast ion conductors are derived from the original Li$_7$P$_3$S$_{11}$ structure. Usually, Li$_7$P$_3$S$_{11}$ is unstable at high temperatures. When the temperature is increased to 420 °C, Li$_7$P$_3$S$_{11}$ decomposes into two fast ion conductors: β-Li$_3$PS$_4$ and Li$_4$P$_2$S$_7$.[50] In Fig. 3b, Li$_7$P$_3$S$_{11}$ is shown as a triclinic structure consisting of PS$_4$ tetrahedra and P$_2$S$_7$ double tetrahedra, where Li-ions are located in the polyhedral cavity.[26] Different preparation methods are reported for the Li$_7$P$_3$S$_{11}$ structure. Li$_7$P$_3$S$_{11}$ obtained by mechanical ball milling and subsequent heat-treatment at 280 °C shows a high conductivity of 3.2×10^{-3} S cm^{-1} at room temperature and low activation energy.[51] Afterward, the conductivity of Li$_7$P$_3$S$_{11}$ can be gradually increased by optimizing the preparation method. The optimized Li$_7$P$_3$S$_{11}$ prepared by hot pressing has a high

Fig. 3 The framework of (a) β-Li$_3$PS$_4$ and (b) Li$_7$P$_3$S$_{11}$ lattices.

conductivity of 1.7×10^{-2} S cm^{-1} at room temperature, almost equivalent to that of liquid organic electrolytes.[21] The low grain boundary resistance during the heat treatment could be the main reason for the high conductivity of the optimized Li$_7$P$_3$S$_{11}$. Another important example for preparing Li$_7$P$_3$S$_{11}$ is the wet chemistry method by a two-step reaction: (1) the formation of solid Li$_3$PS$_4$·ACN phase and amorphous "Li$_2$S–P$_2$S$_5$" phase in liquid phase and (2) the subsequent conversion between the two phases. The conductivity of the as-prepared Li$_7$P$_3$S$_{11}$ sample reaches as high as 8.7×10^{-4} S cm^{-1} at room temperature.[52]

Although positive and effective progress has been made to enhance the conductivity of Li$_2$S–P$_2$S$_5$ binary systems, some problems still remain at present: (1) poor chemical stability: S-SEs are extremely sensitive to moisture and easily react with steam in the air to produce toxic H$_2$S gas and destroy the structure of sulfides.[17] (2) The cost of S-SEs with Li$_2$S as raw material is high. (3) Compatibility between S-SEs and the cathode materials of lithium secondary batteries is poor, which will be further discussed in a following section. Therefore, regulating the components of S-SEs by introducing oxides and phosphate is an effective way to increase the chemical stability. For example, Li$_2$O–Li$_2$S–P$_2$S$_5$ prepared by replacing partial Li$_2$S with Li$_2$O could effectively inhibit the generation of H$_2$S gas.[53] 70% Li$_2$S–29% P$_2$S$_5$–1% Li$_3$PO$_4$ system, after doping Li$_3$PO$_4$ into 70% Li$_2$S–30% P$_2$S$_5$, shows a high conductivity of 1.87×10^{-3} S cm^{-1} at room temperature and enhanced chemical stability.[27] As for cost, seeking new raw materials or exploring new preparation methods could be fundamental solutions.

2.2.1.2 Li$_2$S–P$_2$S$_5$–MeS$_2$ ternary system. Recently, typical thio-LiSICON structure Li$_{10}$GeP$_2$S$_{12}$ (abbreviated as LGPS afterward) was developed, with an extremely high conductivity of 1.2×10^{-2} S cm^{-1} at 27 °C, which is comparable to or higher than those of the liquid organic electrolytes currently used in commercial Li-ion batteries.[38] As indicated in Fig. 4a, LGPS consists of (Ge$_{0.5}$P$_{0.5}$)S$_4$ tetrahedra, PS$_4$ tetrahedra, LiS$_4$ tetrahedra and LiS$_6$ octahedra. (Ge$_{0.5}$P$_{0.5}$)S$_4$ and LiS$_6$ form a 1D chain along the *c*-axis by sharing a common edge. These 1D chains are connected to each other by the PS$_4$ tetrahedra, which are connected to the LiS$_6$ octahedra through a shared angle. Fig. 4b shows the 1D conduction pathways of Li-ions along the *c*-axis in superionic conductors. Indeed, the addition of Ge element in Li$_2$S–P$_2$S$_5$ system could greatly improve the conductivity. However, at the same time, the stability of LGPS against metal lithium is reduced due to the oxidation property of Ge^{4+}. This

Fig. 4 (a) Framework structure of LGPS; (b) Li$^+$ conduction pathways in LGPS; (c) crystal structure of Li$_{9.54}$Si$_{1.74}$P$_{1.44}$S$_{11.7}$Cl$_{0.3}$; (d) nuclear distributions of Li atoms in Li$_{9.54}$Si$_{1.74}$P$_{1.44}$S$_{11.7}$Cl$_{0.3}$ at 25 °C. Reproduced with permission.[37,38] Copyright© (2011, 2016), Springer Nature.

means that the interfacial stability against metal lithium is still limited for LGPS.[28]

Of course, the cost factor is important for wide application of S-SEs in batteries and the price of Ge element is still high.[54] From theoretical calculations, the isovalent cation substitution of Ge^{4+} has minor impact on the intrinsic properties of LGPS.[55] Therefore, the replacement of Ge with tetravalent cations may reduce the cost of S-SEs. Here, Li$_{10}$SiP$_2$S$_{12}$ and Li$_{10}$SnP$_2$S$_{12}$ have similar structure, electrochemical stability and Li-ion conductivity to LGPS. After replacing Ge^{4+} with Sn^{4+}, Li$_{10}$SnP$_2$S$_{12}$ shows a high conductivity of 4×10^{-3} S cm^{-1} at room temperature and the cost is only one-third that of the Li$_2$S–GeS$_2$–P$_2$S$_5$ system.[39] The Ge can be also replaced with Si by high pressure method and the obtained Li$_{11}$Si$_2$PS$_{12}$ shows a high conductivity of 2.3×10^{-3} S cm^{-1} at room temperature.[56] Multi-components could be a good strategy for manipulating the conductivity of S-SEs. In particular, halogen elements in the multi-components are demonstrated to be effective for improving the conductivity. For example, the multi-component Li$_{9.54}$Si$_{1.74}$P$_{1.44}$S$_{11.7}$Cl$_{0.3}$ with a remarkably high conductivity of 2.5×10^{-2} S cm^{-1} at 25 °C was reported, which was the highest value so far for thio-LiSI-CONs.[37] It was demonstrated from the anisotropic thermal displacement of lithium (Fig. 4c) and nuclear density distribution (Fig. 4d) that three-dimensional (3D) conduction pathways of Li ions (1D along the c-axis and 2D in the a–b plane) can be formed in Li$_{9.54}$Si$_{1.74}$P$_{1.44}$S$_{11.7}$Cl$_{0.3}$, superior to the unique 1D pathway of the LGPS family. Therefore, the formation of widely distributed 3D conduction pathways in Li$_{9.54}$Si$_{1.74}$P$_{1.44}$S$_{11.7}$Cl$_{0.3}$ may contribute to its highest ionic conductivity at room temperature.

The distribution of commonly used ternary S-SEs in the Li$_2$S–GeS$_2$–P$_2$S$_5$ ternary phase diagram is illustrated in Fig. 5. Clearly, the Li$_2$S is dominant in the commonly used sulfide electrolytes ($\geq$50% molar ratio); lower P$_2$S$_5$ and GeS$_2$ contents are used here to manipulate the crystallographic structure and intrinsic features. Among all the S-SEs, thio-LiSICONs are the most promising electrolytes for all-solid-state lithium secondary batteries, due to their unique structures and high ionic conductivity at room temperature. Although the conductivity of thio-LiSICONs is comparable to or even higher than those of organic liquid electrolytes, their chemical stability and compatibility with cathode materials are still unsatisfactory, which could undermine the practical application of S-SEs in all-solid-state batteries and urgently needs to be solved.

2.2.2 Argyrodite type. The mineral argyrodite, with a cubic structure and a typical chemical formula of Ag$_8$GeS$_6$, has the high ionic conductivity of Ag-ions. When Ag-ions are replaced by other cations, the original cubic structure still remains for argyrodite type compounds.[57–67] So far, a novel "Li argyrodite" compound in the form of Li$_7$PS$_6$ has a high ionic conductivity. Here, Li$_7$PS$_6$ exists as a cubic phase at high temperatures (HT) and is converted to an orthorhombic phase at low temperatures. The partial substitution of S^{2-} by halogen anions can stabilize the cubic HT phase at room temperature, resulting in good conductivity of about 10^{-3} S cm^{-1}.[68–70] Typical examples are the halogen-substituted argyrodites Li$_6$PS$_5$X (X = Cl, Br, and I). First, argyrodite-type solid electrolytes Li$_6$PS$_5$X were prepared by Dei-seroth et al.[71] As shown in Fig. 6, the stacking structure in Li$_6$PS$_5$X is made of regular octahedral Li$_6$S and tetrahedral PS$_4$ units.[72] The preparation method of Li$_6$PS$_5$X is similar to that of thio-LiSICONs
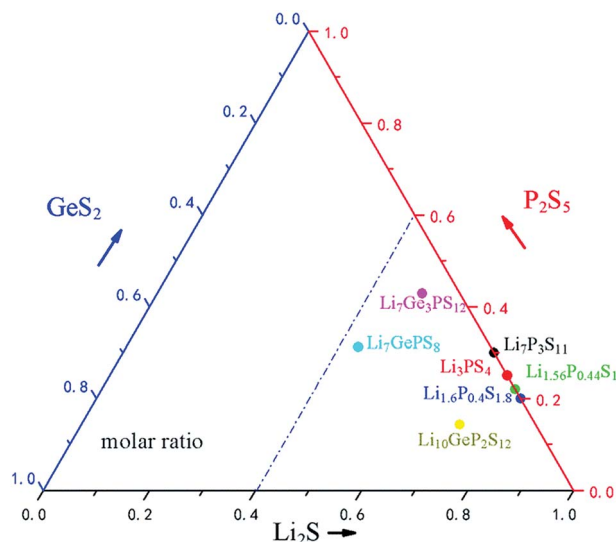
Fig. 5 $Li_2S–P_2S_5–GeS_2$ ternary phase diagrams.

Fig. 7 Thermal evolution of ionic conductivity for different types of solid electrolytes. Reprinted with permission.[81] Copyright© 2018, Royal Society of Chemistry.

and most are prepared by ball milling. For the Cl-substituted sample, Li_6PS_5Cl prepared by ball milling could reach 1.33×10^{-3} S cm^{-1} at 25 °C and have an electrochemical window as high as 7 V (vs. Li/Li$^+$).[42] In the meantime, Li_6PS_5X compounds could also be prepared by mechanical milling with subsequent annealing at 550 °C for 5 h.[73–79] In this preparation process, only Li_2S, P_2S_5 and LiX components can be observed after mechanical milling. The conductivities of Li_6PS_5Cl, Li_6PS_5Br and Li_6PS_5Cl before annealing are 3.3×10^{-5}, 3.2×10^{-5} and 2.2×10^{-4} S cm^{-1}, respectively, at room temperature. After subsequent annealing, the argyrodite phase is finally formed by transformation and crystallization. The conductivities of annealed Li_6PS_5Cl and Li_6PS_5Br increase to 1.9×10^{-3} and 6.8×10^{-3} S cm^{-1}, respectively, at room temperature, while that of Li_6PS_5I is reduced to 4.6×10^{-7} S cm^{-1}. Here, the activation energy for Li-ion diffusion in Li_6PS_5Cl and Li_6PS_5Br is lower, contributing to the high conductivities. It is also reported that Cl$^-$ and Br$^-$ can disorder S^{2-} to promote Li-ion mobility, while I$^-$ cannot exchange with S^{2-} due to its large size. Therefore, Li_6PS_5I cannot be comparable with Li_6PS_5Cl and Li_6PS_5Br on conductivity.[75] In particular, the Li_6PS_5Cl and Li_6PS_5Br obtained by solid-state sintering processes with an excess of Li_2S are demonstrated to be superior, exhibiting higher conductivities of 1.8×10^{-3} and 1.3×10^{-3} S cm^{-1}, respectively, at room temperature.[80]
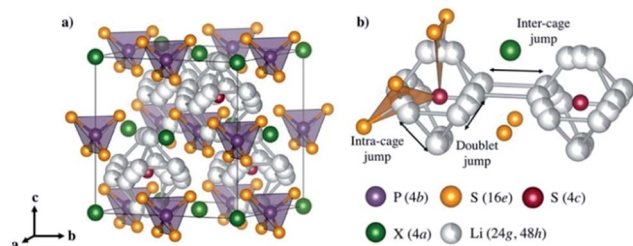

Fig. 6 (a) Crystal structures of Li_6PS_5X with X = Cl, Br, and I. (b) Lithium ion transport mechanism. Reproduced with permission.[72] Copyright© 2017, American Chemical Society.

Argyrodite type solid electrolytes are very promising for all-solid-state batteries based on the considerations of conductivity and cost. However, similar to most S-SEs, the argyrodite type solid electrolytes are very sensitive to moisture, which should be the main focus for future applications.

To sum up, a wide variety of S-SEs with high conductivities has been reported, with thermal evolution of ionic conductivity drawn in Fig. 7. Here, high conductivity (higher than 10^{-3} S cm^{-1} at room temperature) is a primary concern for solid electrolytes to be used in all-solid-state lithium secondary batteries. It can be seen that there are only a few electrolyte systems that can meet the demand of high conductivity: $Li_{9.54}Si_{1.74}P_{1.44}S_{11.7}Cl_{0.3}$, $Li_{10}GeP_2S_{12}$, doped-Li_3N, $Li_{3.25}GeP_{0.75}S_4$, $Li_2S–SiS_2–Li_3PO_4$, $Li_{14}Zn(GeO_4)_4$, and $Li_7P_3S_{11}$. Among all the electrolytes, $Li_{14}Zn(GeO_4)_4$ is stable, but not ideal due to its excessive hardness and poor compatibility with electrode materials. For the doped-Li_3N sample, ion conductivity is satisfactory, but the low decomposition voltage and extreme sensitivity toward moisture are insurmountable at present. The applications of obtained $Li_{9.54}Si_{1.74}P_{1.44}S_{11.7}Cl_{0.3}$, $Li_{3.25}GeP_{0.75}S_4$ and $Li_2S–SiS_2–Li_3PO_4$ are largely limited due to their hard preparation processes and complex elemental components. It seems that every family of these electrolytes has problems currently. Comparatively speaking, $Li_{10}GeP_2S_{12}$ and $Li_7P_3S_{11}$ are the most promising solid electrolytes for high performance all-solid-state lithium secondary batteries due to their high conductivities and simple preparation process. Of course, there is still great room for improvement of conductivity in solid electrolytes, so it is necessary to explore new electrolyte systems based on the requirement of high conductivity.

3 S-SE's application in all-solid-state lithium batteries

With constant progress in highly conductive solid electrolytes, the developments in all-solid-state lithium secondary batteries

Fig. 8 Comparison of (a) commercial Li-ion batteries, (b) all-solid-state Li-ion batteries and (c) all-solid-state Li–S batteries.

change rapidly. The schematic structures of three commonly used lithium batteries with solid electrolytes are shown in Fig. 8.[82] The first advantage of all-solid-state batteries is high safety, due to their simplified structure and the excellent mechanical properties of solid electrolytes. Another outstanding advantage of all-solid-state lithium batteries is their high theoretical energy density.[83–85] The energy density of all-solid-state lithium batteries could reach 300–600 W h kg^{-1}, which is much higher than commercial liquid batteries at about 200 W h kg^{-1}.[85–88] The reasons are as follows:

(1) Lithium has the lowest electrode potential and the lowest molar mass and its theoretical specific capacity can reach 3860 mA h g^{-1}.[89,90] The compatibility of the S-SEs with lithium is better than that of liquid electrolytes with lithium, because of fewer side reactions on the interface. Therefore, lithium can be used as the anode in all-solid-state batteries, which is helpful to increase the volumetric and gravimetric energy densities of all-solid-state batteries.

(2) Solid electrolytes usually have a wide electrochemical window. When combined with suitable cathode materials, the battery could provide a high operation voltage to improve the energy density.[38,87,88]

Although the ionic conductivity of S-SEs is competitive to those of liquid electrolytes, the electrochemical performance of all-solid-state lithium batteries is still unsatisfactory, highly depending on the interface issues between electrodes and S-SEs.[91] There are several key issues of S-SE application in all-solid-state lithium batteries: (1) A solid–solid contact interface is formed between the electrode and electrolyte, but is not stable enough; (2) the volume change of the electrode during charge and discharge is unavoidable, which further destroys the electrode/electrolyte interface; (3) the chemical stability of S-SEs is poor. It was mentioned above that the chemical stability can be effectively improved to a certain extent by manipulating the composition of the electrolytes and optimizing the preparation process. However, the issue of solid–solid interfaces between electrodes and electrolytes is unavoidable in all-solid-state batteries[92] and should be paid more attention.

3.1 Interface layer and interface impedance

In all-solid-state lithium batteries, the interface between the electrolytes and electrodes has significant influence on the working mechanism and electrochemical performance.[93–97] In particular, no wettability exists among solids; the contact between solid and solid is not comparable with that of solid and liquid, leading to large interfacial impedance between solid electrolytes and electrodes. The space charge layer model, proposed by Takada *et al.*, is popular to explain the interfacial impedance between the S-SEs and oxide cathode materials in all-solid-state lithium batteries.[98] Another explanation for the interface phenomenon is mutual diffusion of different elements in oxide electrodes and S-SEs.[99]

3.2 Problems and current situation of the interface between oxide cathodes and sulfide solid electrolytes

The concept of a space charge layer was initially proposed based on a pioneering work on solid-state reactions, where the interface between two F$^-$ ion conductors of BaF_2 and CaF_2 was studied. It was demonstrated that partial F$^-$ ions can be transferred from one side to the other to reach equilibrium state under the driving force of different chemical potentials, resulting in the formation of vacancies and interstitial ions. Both the vacancies and interstitial ions help enhance ion conduction at the interface. This phenomenon was referred to as "nanoionics".[100,101]

Takada *et al.* introduced the nanoionic phenomenon into the interface between oxide electrodes and S-SEs, forming a space-charge layer.[91] The space-charge layer on the interface between oxide cathodes and S-SEs is harmful for cation transfer. This is a common feature of good ionic conductivity for both cathode materials and S-SEs. However, the electron insulation is absolute for S-SEs, while the good electron conductivity is also suitable for cathode materials. Currently, commercial cathode materials with large capacity are generally Ni-rich oxides with high electrode potentials. When contacting both oxide cathode materials and S-SEs, Li-ions move from S-SEs to the oxide under the driving force of chemical potential difference between the two materials. Correspondingly, the migration of Li-ions results in formation of the space-charge layer on the interface between S-SEs and oxide cathode. Specifically, the composition and structure of S-SEs on the interface are changed, leading to lower ion conductivity and increasing the interfacial resistance. However, the space charge layer on the cathode side of the oxide interface disappears rapidly because electrons simultaneously neutralize excess Li-ions. Therefore, the space charge layer is usually formed in the S-SE side on the interface between cathode and S-SE (as shown in Fig. 9).[98] The formation of the space charge layer has great impact on the performance of all-solid-state lithium batteries.

Thus, to improve the electrochemical performance of all-solid-state lithium batteries, reducing the impact of the space charge layer is imperative. Takada proposed a buffer layer to alleviate development of the space charge layer.[84] Inserting an additional oxide layer as an ion-conductive and electron-insulated buffer layer between the oxide cathode and S-SEs is
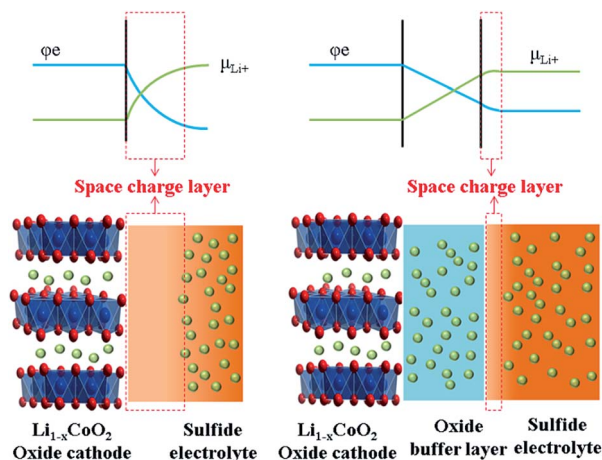
Fig. 9 Formation of the space charge layer and a modification mechanism with a buffer layer.

Fig. 10 All-solid-state lithium batteries with (a) metal anode and (b) powder anode.

an effective way to slow the impact of the space charge layer.[91,102] Correspondingly, two interfaces are formed after introducing the buffer layer: one between the mixed-conducting oxide cathode and ion-conductive oxide and the other between the ion-conductive oxide and S-SEs. The space charge layer at both interfaces could be inhibited to a certain extent. The additional oxide layer avoids direct contact between oxide cathode and S-SEs as a buffer, so it is called a buffer layer. Take $LiCoO_2$ and S-SEs as examples, as shown in Fig. 9. The space charge layer is largely developed when S-SEs are in direct contact with the $LiCoO_2$. With a buffer layer between $LiCoO_2$ and S-SEs, the space charge layer is greatly suppressed.

Therefore, it is important to search for suitable buffer layer materials to improve the performance of all-solid-state batteries. Electrodes in all-solid-state lithium batteries are usually mixtures of active materials, conductive additives and S-SEs. Here, the buffer layer should be formed on the surface of active materials before mixture. The current investigation shows that the mass ratio of $Li_{10}GeP_2S_{12}$ and $LiCoO_2$ in the composite cathodes is usually between 20/80 and 30/70 for better electrochemical performance.[92] In the future, the content of S-SEs as inactive materials in the electrode should be manipulated as low as possible to maintain the high energy density of all-solid-state lithium batteries. For effective transport of ions and conduction of electrons, the interface between electrodes and S-SEs could be constructed as a gradient. This special gradient transition layer would help stabilize the interface and improve the performance of all-solid-state lithium batteries. Fig. 10 shows more details about the interface structure and gradient transition layer for all-solid-state lithium batteries, as well as the composite cathode, Li anode and S-SEs.

Next, the interfacial problems between S-SEs and oxide cathodes will be discussed for different oxide cathodes in all-solid-state lithium batteries.

3.2.1 Layered $LiCoO_2$ cathode material. $LiCoO_2$ is commonly used as a cathode material for lithium-ion batteries in portable devices due to its electrochemical stability, high structural stability and high tap density.[103–105] Many attempts to

reduce the interfacial resistance by inserting different buffer materials on $LiCoO_2$ have been made in the past. $LiNbO_3$ is demonstrated to be a typical buffer material due to its high ionic conductivity. All-solid-state batteries are usually assembled with $LiNbO_3$-coated $LiCoO_2$ as cathode, $Li_{3.25}Ge_{0.25}P_{0.75}S_4$ as electrolyte and In–Li alloy as anode.[98,106] The interface resistance is reduced by two orders of magnitude after coating with $LiNbO_3$, contributing to the great improvement of the electrochemical performance of the batteries. Similarly, all-solid-state batteries can be also built with $Li_{10}GeP_2S_{12}$ as electrolyte, In–Li alloy as anode, and TaO_3-coated $LiCoO_2$ as cathode.[107] The interface resistance is reduced from 3×10^5 to 4×10^3 Ω cm^{-2} after coating the TaO_3 buffer layer on the cathode. In addition, Li_2SiO_3 can be considered as a buffer layer to deposit on $LiCoO_2$. It was shown that a buffer layer of 0.06 wt% Li_2SiO_3 effectively reduces the interface impedance and improves the electrochemical performance of the all-solid-state battery with $Li_2S–P_2S_5$ as electrolyte (Fig. 11a and b).[99,108] As characterized by STEM (Fig. 11c and d), a thick interfacial layer is formed between $LiCoO_2$ and $Li_2S–P_2S_5$, leading to large interfacial impedance and poor electrochemical performance due to mutual diffusion and interactions of Co, P, and S. After coating the Li_2SiO_3 buffer layer, a small interfacial impedance and large discharge capacity can be simultaneously obtained. Importantly, the interface of $LiCoO_2/Li_2S–P_2S_5$ layer is thin and clean with the appearance of Si.

In a similar way, S-SEs can be coated onto active materials to form a favourable electrode–electrolyte interface and increase the electrochemically active surface area.[109] As shown in Fig. 12, S-SEs-coated $LiCoO_2$ exhibits larger discharge capacity and better rate performance compared to a simple mixture of $LiCoO_2$ and S-SEs. The effects of different grain size and composition of active materials on the electrochemical performance of all-solid-state batteries are also explored. In particular, the composition of 10 : 1 weight ratio of 10 μm to 1.7 μm $LiCoO_2$ helps to show better performance, for which the solid–solid contact/interface should be optimized.

3.2.2 Spinel cathode materials. Spinel cathode materials ($LiMn_2O_4$ and $LiNi_{0.5}Mn_{1.5}O_4$) possess the advantages of low

This journal is © The Royal Society of Chemistry 2019

J. Mater. Chem. A, 2019, 7, 20540–20557 | 20547

Fig. 11 (a) Impedance profiles of the all-solid-state cells $In/Li_2S–P_2S_5$ with solid electrolyte non-coated and Li_2SiO_3-coated $LiCoO_2$ at $-30\,°C$ after charging to 3.6 V *vs.* Li−In. (b) Discharge curves of the all-solid state cells under the current density of 0.064 mA cm^{-2} at 30 °C. (c) Cross-sectional HAADF-STEM image of $LiCoO_2$ electrode/$Li_2S–P_2S_5$ solid electrolyte interface after initial charging and cross-sectional EDX line profiles for Co, P, and S elements. (d) Cross-sectional HAADF-STEM image of the Li_2SiO_3-coated $LiCoO_2$/$Li_2S–P_2S_5$ interface after initial charging and cross-sectional EDX line profiles for Co, P, S, and Si elements.[99,108] Reproduced with permission. Copyright© (2009, 2010), American Chemical Society.

Fig. 12 (a) Volume fractions of respective materials along the electrode thickness; (b) electrochemical performance of S-SE-coated $LiCoO_2$ and $LiCoO_2$ + S-SE; (c) S-SE-coated $LiCoO_2$ particles with different grain sizes; (d) electrochemical performances of different cathode compositions. Reproduced with permission.[109] Copyright© 2017, Royal Society of Chemistry.

cost, good safety and high voltage platform as high as 4.7 V.[110–112] For application of spinel cathodes in all-solid-state batteries, a buffer layer is still essential. For example, $LiMn_2O_4$ can be coated with $Li_4Ti_5O_{12}$ by sol–gel method. Correspondingly, the interfacial impedance of cathode/electrolyte can be greatly reduced after coating with $Li_4Ti_5O_{12}$ film and the electrochemical performance of the assembled In/$80Li_2S–20P_2S_5$/$LiMn_2O_4@Li_4Ti_5O_{12}$ batteries is improved as well.[113] Amorphous-Li_3PO_4-deposition on $LiMn_2O_4$ cathode by pulsed laser deposition is also effective for decreasing the interfacial resistance and releasing a larger reversible capacity of 62 mA h g^{-1}.[114] As for the high voltage $LiNi_{0.5}Mn_{1.5}O_4$ cathode, $LiNbO_3$ seems to be a more suitable buffer layer material based on safety considerations.[115]

3.2.3 Layered ternary oxide cathode materials. The ternary oxide cathode materials of the general formula $LiNi_xCo_y$-$M_{1-x-y}O_2$ (M = Mn, Al) have been popular in recent years due to their advantages of high specific capacity, low cost, and environmental friendliness.[117–119] Specifically, nickel-rich oxide cathode (NCM811) with multi-electron reaction and high reversible capacity was introduced into all-solid-state batteries.[116] As presented in Fig. 13, the capacity loss of NCM811 cathode in the first cycle is serious, caused by a change in the chemical composition at the S-SEs/cathode interface and shrinkage of NCM particles during delithiation. It means that

the destruction at the S-SEs/cathode interface in the first cycle is final and not correctable in the following cycles, resulting in the rapid drop of the reversible capacity of NCM811 cathode without any coating buffer layer. After coating the $LiAlO_2$ buffer layer on $LiNi_{1/3}Co_{1/3}Mn_{1/3}O_2$ (NCM333) by sol–gel method and ultrasonic treatment, the battery with $LiAlO_2$-coated NCM333 as cathode, Li_3PS_4 as electrolyte and $Li_{4.4}Si$ alloy as anode was assembled and investigated.[120] It is demonstrated that 1.0 mol%
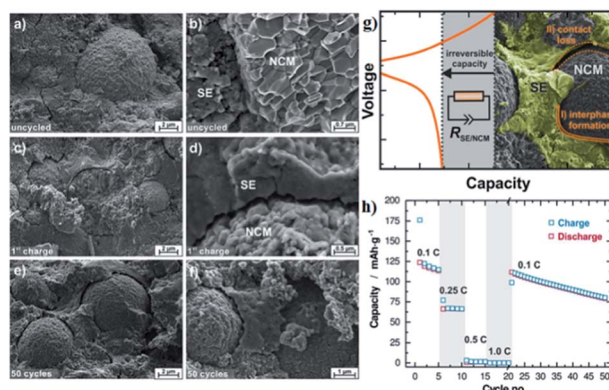

Fig. 13 (a and b) Scanning electron micrographs of the cathode composite of NCM811 and $β-Li_3PS_4$ as prepared in a solid-state cell but without the application of current or potential. (c and d) SEMs of a Li−In|$β-Li_3PS_4$|NCM-811 batteries after single charging to 4.3 V *vs.* Li/Li$^+$ at 0.1 C. (e and f) SEMs of a given cell after 50 full battery cycles in the discharged state. (g) Schematic diagram of performance degradation mechanism in all-solid-state batteries. (h) Rate test and long-term cyclability for the all-solid-state batteries. Reproduced with permission.[116] Copyright© 2017, American Chemical Society.

20548 | *J. Mater. Chem. A*, 2019, **7**, 20540–20557

This journal is © The Royal Society of Chemistry 2019

$LiAlO_2$ coating is good enough for NCM333 cathode to release a high initial discharge capacity of 134 mA h g^{-1} and to retain good capacity after 400 cycles.

The nickel-rich oxide $LiNi_{0.8}Co_{0.15}Al_{0.05}O_2$ (NCA) cathode is also verified in all-solid-state batteries. As shown in Fig. 14, after coating a thin layer of Li_2O–ZrO_2 (8 nm),[121] all-solid-state batteries with Li_2O–ZrO_2-coated NCA as cathode, $80Li_2S$–$20P_2S_5$ as electrolyte, and In–Li alloy as anode can be charged/discharged repeatedly with good capacity retention. The NCA can be also coated with $Li_4Ti_5O_{12}$ (LTO) for verification in all-solid-state batteries.[122] The battery with $Li_4Ti_5O_{12}$-coated NCA cathode shows a discharge capacity of about 110 mA h g^{-1}, superior to that (70 mA h g^{-1}) of the non-coated cathode.

The effects of the particle size and structure defects of oxide cathodes in all-solid-state batteries are also important. First, reducing the particle size of the cathode materials by ball milling is helpful to form sufficient contact between the electrolytes and cathode.[123,124] Secondly, a subsequent heat treatment on the ball-milled cathode materials can further reduce structural defects on the surface of the cathode materials. Thereby, the electrochemical performance of the all-solid-state battery can be improved to some extent. Typically, all-solid-state batteries with NCA, ball-milled NCA, and heat-treated NCA as cathodes are built. The interface impedances are 652, 480 and 198 Ω cm^{-2} and the initial discharge capacities of the cathodes are 46.7, 89 and 146 mA h g^{-1}, respectively.

In all-solid-state lithium ion batteries, the interface compatibility between the oxide cathode materials and S-SEs should be a key issue. It is imperative to probe the reaction mechanism of the interface and find a strategy for stabilizing the interface. The commonly used buffer layer materials are summarized in the following categories according to their structure and composition (Fig. 15): spinel oxides, perovskite oxides, lithium salts, and general oxides. At first, the commonly used buffer materials have been general oxides. Although the development of the space charge layer can be suppressed to a certain extent, the rate performance of the battery is undermined due to the insulating properties of the oxide buffer layer. Compared with general oxides, lithium salts have good ion-conducting properties, leading to better rate performance of all-solid-state batteries. According to the above classification, typical examples of the three types are $Li_4Ti_5O_{12}$, Li_3PO_4 and $LiNbO_3$. A certain amount of $Li_4Ti_5O_{12}$ coating on the cathode surface could effectively suppress the formation of the space

Fig. 15 Summary of buffer layer materials. Produced from experimental data.

charge layer.[125] But due to its low ionic conductivity (10^{-9} S cm^{-1}), the resistance of the coating layer itself became predominant in the electrode resistance, thus limiting the electrochemical performance of all-solid-state batteries. Li_3PO_4 has a higher ionic conductivity of 10^{-8} S cm^{-1}; thus, a Li_3PO_4 buffer layer could lead to better performance.[126] $LiNbO_3$ is an excellent material for the buffer layer in place of $Li_4Ti_5O_{12}$ and Li_3PO_4 because of its extremely high ionic conductivity of 10^{-5} to 10^{-6} S cm^{-1} in amorphous state and its good stability.[102] It effectively reduces interfacial resistance and improves the high-rate capability of all-solid-state batteries. For buffer layer materials, high ionic conductivity, good chemical stability and electrochemical passivation feature should be considered, as well as low cost and insensitivity to moisture. Of course, $LiNbO_3$ seems to be effective as a buffer layer for all the oxide cathode materials in all-solid-state lithium ion batteries.

4 S-SE application in all-solid-state lithium–sulfur battery

4.1 Lithium–sulfur battery

Sulfur is a light-weight element which can react with lithium to form Li_2S through a two-electron reaction, leading to the high theoretical specific capacity of 1672 mA h g^{-1},[127–131] which is about five times that of current commercial transition metal oxide cathode materials.[132–137] However, there are several major problems in conventional liquid lithium–sulfur (Li–S) battery: (1) poor ionic conductivity and electrical conductivity of sulfur and its discharge product Li_2S; (2) large volume expansion (~79%) from S to Li_2S; (3) dissolution of intermediate polysulfide, resulting in a shuttle effect and poor cycle performance; (4) flooded organic electrolyte, leading to low energy density; (5) flammability and leakage of the organic electrolyte. In order to improve the electrochemical performance, energy density, and safety, it is effective to build all-solid-state Li–S batteries. S-SEs could be good
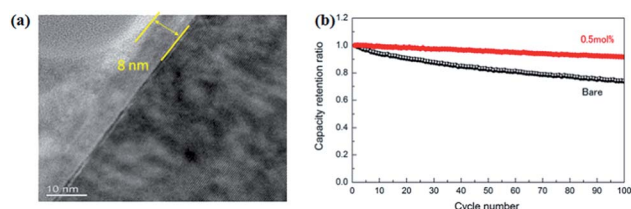

Fig. 14 (a) TEM image of a cross section of a 0.5 mol% LZO coated NCA particle. The right hand (dark) side corresponds to NCA; (b) cycle characteristics of bare and 0.5 mol% LZO coated NCA at 25 °C. Reproduced with permission.[121] Copyright© 2013, Elsevier B.V.

candidates for an all-solid-state Li–S battery. In particular, there is good compatibility between S-SEs and sulfur, without the space charge layer effect mentioned in the previous section.

4.2   Research progress on all-solid-state lithium–sulfur battery

Although solid electrolytes can effectively suppress the shuttle effect of soluble intermediate polysulfide, there are still some problems with all-solid-state Li–S battery. First, due to the immobile nature of the solid electrolyte, the volume expansion caused by sulfur in the charge and discharge processes induces great stress at the electrode/electrolyte interface, damaging the structure of the interface. Second, the electron conductivities of S and Li_2S are extremely poor, severely limiting the electrochemical performance of the all-solid-state Li–S battery. Third, the contacts among S/Li_2S, conductive additives and solid electrolytes are insufficient. Therefore, it is urgent to search for suitable materials or modified methods to solve these problems in the all-solid-state Li–S battery.

Building nanocrystals and nanostructures is an effective way to improve the above problems.[138] First, the nanostructure has a large specific surface, so sufficient contact between the active materials and solid electrolytes can be formed based on the large surface. Second, although the poor conductivity of S and Li_2S limits the depth of the electrochemical reaction, nanocrystals with many active sites can improve the utilization of sulphur active material. In the meantime, the nanostructure can accommodate the pressure introduced during repeated cycling.

4.2.1   Sulfur cathode.
Due to the poor electronic and ionic conductivities of sulfur, electronic conductive materials and solid electrolytes should be homogeneously mixed with the sulfur.[139,140] Generally, carbon materials have good electrical conductivity and large specific surface area, so the combination of carbon materials and sulfur could be a good choice for improving the conductivity of the composite cathode. Previously, common carbon materials have been reported for the all-solid-state Li–S battery, including acetylene black (AB),[141] Ketjen black (KB),[142] activated carbon (AC),[143] and vapor grown carbon fibers (VGCF).[144]

Sulfur–AB composite cathodes prepared by ball-milling were used to build all-solid-state batteries.[145] The all-solid-state battery, assembled with a sulfur–AB composite cathode, can deliver a large capacity of 996 mA h g^{-1} at 0.64 mA cm^{-2} and retain a capacity of 853 mA h g^{-1} at 1.3 mA cm^{-2} after 200 cycles. After further optimization with small particle size and sufficient contact between S and AB,[146] the sulfur–AB composite cathode shows a large initial discharge capacity of 1087 mA h g^{-1} with a coulombic efficiency of 97% and maintains a reversible capacity of 1050 mA h g^{-1} at 0.064 mA cm^{-2} after 50 cycles. In addition, the composite cathodes using VGCF[144] and AC[147] as conductive additives also exhibit better electrochemical performance. Similar to carbon materials, metal sulfides (such as CuS_2)[139] and conductive polymers (such as polyacrylonitrile)[148] are also commonly used to construct composite cathodes.

4.2.2 Li_2S cathode.
Similar to sulfur, Li_2S has a high theoretical capacity of ~1166 mA h g^{-1}. In addition, Li_2S is highly sensitive to moisture and oxygen, which makes the preparation process of the cathode materials more complicated.[130,138,149,150]

As mentioned above, constructing a composite cathode with conductive additive, solid electrolytes and Li_2S is a good solution to improve the performance of Li_2S. The optimal preparation process of the composite cathode with Li_2S, AB and S-SEs is explored by mechanical ball milling.[138] As indicated in Fig. 16, the Li_2S–AB–S-SEs composite cathode can be prepared by ball milling, which is superior for capacity and cycle stability compared with manual grinding. Specifically, the Li_2S–AB–S-SEs cathode has a discharge platform of 2 V (vs. Li), which corresponds to the reaction of $Li_2S = S + 2Li^+ + 2e$, proving the generation of polysulfide is suppressed. The initial charge and discharge capacities of the all-solid-state batteries with the Li_2S–AB–S-SEs composite cathode are 1010 and 920 mA h g^{-1}, respectively. To increase the utilization of the Li_2S active material, the effects of the particle size of Li_2S active materials on the reversible capacity and rate performance of all-solid-state batteries are also investigated. Clearly, reducing the particle size of Li_2S active materials is helpful to improve the electrochemical performance of all-solid-state Li–S batteries.

It is also feasible to improve the performance of Li_2S by designing a special structure. A core–shell structure with nano-Li_2S as the core and Li_3PS_4 as the shell is obtained and has an ionic conductivity of 10^{-7} S cm^{-1} at 25 °C, almost 6 orders of magnitude higher than that of bulk Li_2S (~10^{-13} S cm^{-1}).[151] As demonstrated in Fig. 17, the all-solid-state battery assembled with the LSS cathode shows an initial discharge capacity of 848 mA h g^{-1} (based on Li_2S) and a capacity retention of about 70% after 100 cycles. The good performance of LSS is ascribed

Fig. 16   SEM images of (a) Li_2S + AB + S-SEs, (b) Li_2S–AB + S-SEs, and (c) Li_2S–AB–S-SEs electrodes. (d) Charge–discharge curves of all-solid-state cells Li–In/80Li_2S–20P_2S_5 glass-ceramic/Li_2S using Li_2S + AB + S-SEs, Li_2S — AB + S-SEs, and Li_2S–AB–SEs as cathodes. SEM images of (e) non-milled Li_2S, (f) Li_2S particles milled for 20 h, and Li_2S–AB–S-SEs electrodes using (g) non-milled Li_2S and (h) milled-Li_2S. (i) Charge–discharge curves for the first cycle of all-solid-state cells with Li_2S–AB–S-SEs electrodes prepared using (e) non-milled and (f) milled Li_2S particles. Reproduced with permission.[138] Copyright© 2012, Royal Society of Chemistry.

20550 | J. Mater. Chem. A, 2019, 7, 20540–20557

This journal is © The Royal Society of Chemistry 2019

Fig. 17 SEM images and elemental maps of the cathode before and after cycling at 60 °C: SEM images of the cathode (a) before cycling and (e) after 100 cycles; (b), (c), and (d) are elemental maps of carbon, sulfur, and phosphorus before cycling; (f), (g), and (h) are elemental maps of carbon, sulfur, and phosphorus after 100 cycles. (i) The schematic diagram of the core−shell structure and voltage−capacity curve of the battery. (j) Electrochemical cycling performance of nano-Li$_2$S and LSS as the cathode materials for all-solid-state Li−S batteries at the rate of C/10 and 60 °C. Reproduced with permission.[151] Copyright© 2013, American Chemical Society.

to its enhanced ionic conductivity after coating with Li$_3$PS$_4$ and reduced interfacial resistance between the electrodes and electrolytes. The high lithium-ion conductivity of LSS results in excellent cycling performance for the all-solid-state Li–S battery, also promoting safety during cycling.

In summary, the insulation of S/Li$_2$S is the main problem hindering the development of the all-solid-state Li–S battery. Intimate contact among electrode components is effective to reduce the particle size and improve the conductivity of composite electrodes to solve the above problems.

4.2.3 Metal sulfides cathode. Recently, transition metal sulfides with unique nanostructures (such as NiS,[152] TiS$_2$,[153] and FeS[154]) have been used as active materials in all-solid-state lithium batteries. These cathodes not only have moderate operating voltages and high theoretical specific capacity, but also better interfacial compatibility and stability with S-SEs. Furthermore, excellent solid–solid interface contact can be achieved by reducing the size of the active material to the nanometer scale. Therefore, transition metal sulfides are promising for high energy density electrode materials.

In order to achieve intimate contact between sulfide electrodes and S-SEs, Fe$_3$S$_4$@Li$_7$P$_3$S$_{11}$ is prepared by *in situ* coating Li$_7$P$_3$S$_{11}$ on Fe$_3$S$_4$.[155] The Fe$_3$S$_4$@Li$_7$P$_3$S$_{11}$ nanocomposites are employed to construct all-solid-state batteries. The all-solid-state batteries (Li/75% Li$_2$S–24% P$_2$S$_5$–1% P$_2$O$_5$/Li$_{10}$GeP$_2$S$_{12}$/Fe$_3$S$_4$@Li$_7$P$_3$S$_{11}$) show superior cycling stability. As shown in Fig. 18, after 200 cycles, the discharge capacity remained a high value of 1001 mA h g^{-1} at a current density of 0.1 A g^{-1}. Subsequently, sulfide nickel anchored carbon nanotube (NiS–CNT) nanocomposites are prepared by a facile hydrothermal

Fig. 18 (a) High magnification SEM, (b) TEM, and (c) HRTEM images of Fe$_3$S$_4$@Li$_7$P$_3$S$_{11}$ nanocomposites; the inset in (c) is the SAED pattern; (d) STEM-EDS elemental mapping images of Fe$_3$S$_4$@Li$_7$P$_3$S$_{11}$ nanocomposites, marked by the rectangular region, for Fe, P, and S. (e) Comparison of the electrochemical performance between Fe$_3$S$_4$@Li$_7$P$_3$S$_{11}$ and pristine Fe$_3$S$_4$. Reproduced with permission. Copyright© 2017.[155] Royal Society of Chemistry.

method.[3] The all-solid-state batteries with NiS–CNT as cathode also deliver high reversible capacity and excellent cycling stability.

5 Current situation of the interface between anode/S-SEs

5.1 Characteristics of metal lithium

Metal lithium is an ideal anode material due to its low standard electrode potential (−3.04 V *vs.* standard hydrogen electrode), low density (0.53 g cm^{-1}) and high theoretical specific capacity of 3862 mA h g^{-1}.[89] Conventional lithium batteries with organic liquid electrolytes have poor compatibility with metal lithium. Metal lithium is extremely reactive and easily forms uncontrolled lithium dendrites at the anode surface, thus leading to internal short-circuiting and serious safety issues.[97,156,157] In all-solid-state lithium batteries, all components are solid. The solid electrolyte has good mechanical properties which can weaken the growth of lithium dendrites during charge/discharge cycling. Therefore, metal lithium can be employed as an anode in all-solid-state lithium batteries with high energy density. Although S-SEs have good mechanical properties, they are electrochemically unstable to metal lithium.[158] It implies

This journal is © The Royal Society of Chemistry 2019

J. Mater. Chem. A, 2019, **7**, 20540–20557 | **20551**

that the interface change between the anode and S-SEs could be serious and strongly related to the performance of all-solid-state batteries. This part will discuss the interfacial problem from two aspects: electrochemical stability and mechanical stability.

5.2 Electrochemical stability of the interface between metal lithium and S-SEs

In fact, most highly-conductive S-SEs (such as $Li_7P_3S_{11}$, $Li_{10}GeP_2S_{12}$, and $Li_{9.54}Si_{1.74}P_{1.44}S_{11.7}Cl_{0.3}$) are unstable against active lithium metal.[37,113,159] To improve electrochemical stability between S-SEs and lithium and to reduce the decomposition of S-SEs, lithium alloys are introduced as anodes.[160,161] Among all the alloys, Li–In alloy with a flat potential platform of 0.62 V (vs. Li/Li$^+$) and a high specific capacity is widely used in all-solid-state lithium batteries to suppress interfacial reactions and the decomposition of solid state electrolytes.[160] Of course, the energy density of all-solid-state batteries can be slightly reduced due to low battery voltage with Li–In alloy as anode. In addition, cost should be a concern for a battery with indium as anode material. Therefore, improving the interfacial stability between the lithium metal and S-SEs to inhibit the growth of Li dendrites is critical for utilization of S-SEs in all-solid-state lithium secondary batteries.

The electrochemical stability can be improved by doping anions into S-SEs. $Li_7P_2S_8I$, prepared by doping LiI in Li_3PS_4, shows extremely high electrochemical stability to a metal lithium anode.[162] Improving the interface between lithium metal anode and S-SEs could be done through the following three aspects: (1) modification on the surface of S-SEs; (2) modification on the surface of metal lithium; (3) introduction of a buffer layer between S-SEs and metal lithium.[35] Among these, the buffer layer solution is the most commonly used. Therefore, the characteristics of different buffer layer materials are explored. 20 nm Si-deposited metal lithium is obtained by laser pulse deposition[163] and the $LiCoO_2|Li_2S-P_2S_5|Li$ battery is then assembled. Here, the battery with bare lithium anode presents a capacity retention rate of 76% after 100 cycles, while the

battery with Si-deposited lithium anode is cycled without capacity decay almost for 1000 cycles. Subsequently, different deposited layers of Si, Al and Sn on the surface of metal lithium are studied.[163] The all-solid-state batteries with Si-deposited lithium anode exhibit optimized electrochemical performance. Employing LiF (or LiI) as a buffer layer at the interface between metal Li and S-SEs and penetrating methoxyperfluorobutane (HFE) or I solution inside S-SEs could effectively suppress Li dendrite growth (Fig. 19).[164] A $LiCoO_2@LiNbO_3/Li_7P_3S_{11}/Li$ all-solid-state battery employing HFE-penetrated $Li_7P_3S_{11}$ glass-ceramic as electrolyte and LiF-coated Li metal as anode shows a high reversible discharge capacity of 118.9 mA h g^{-1} at 0.1 mA cm^{-2} and retains 96.8 mA h g^{-1} after 100 cycles.

5.3 Mechanical stability of the interface between metal lithium and S-SEs

Another important problem is the formation of Li dendrites along the voids and grain boundaries in solid electrolytes, although these materials have much stronger mechanical strength than Li metals.[157] In fact, there are problems similar to lithium dendrite growth in solid electrolytes. The mechanism for dendrite formation and growth in solid electrolytes is still unclear and controversial.

Metal lithium reacts and grows along grain boundaries and cracks inside the S-SEs.[157] However, lithium dendrites are still formed and grown in the glassy sulfide electrolytes without a grain boundary.[165] In order to suppress the growth of Li
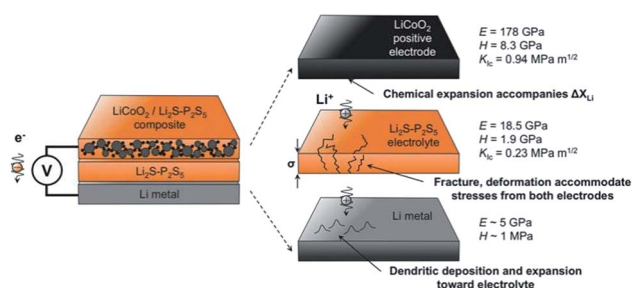

Fig. 20 Summary of mechanical performance data for $Li_2S-P_2S_5$ (LPS) in the context of all-solid-state batteries. Reprinted with permission.[166] Copyright© 2017, John Wiley and Sons.
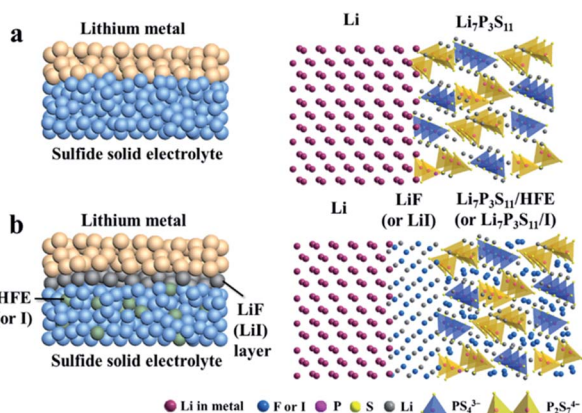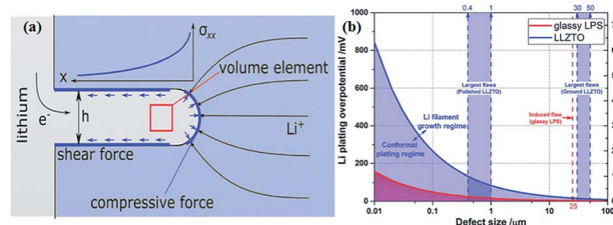

Fig. 21 (a) The effect of stress accumulation on lithium growth; (b) inverse square root dependence of Li plating over-potential and crack-extension stress ($\sigma_{0,max}$) on defect size of glassy LPS and LLZTO. Reproduced with permission.[165] Copyright© 2017, John Wiley and Sons.

Fig. 19 Schematic diagrams of (a) $Li/Li_7P_3S_{11}$ interface of ASSLIBs and (b) modified interface with a uniform thin LiF (or LiI) interphase layer and HFE (or I solution) infiltrated sulfide electrolyte. Reprinted with permission.[164] Copyright© 2018, Elsevier B.V.

20552 | J. Mater. Chem. A, 2019, 7, 20540–20557

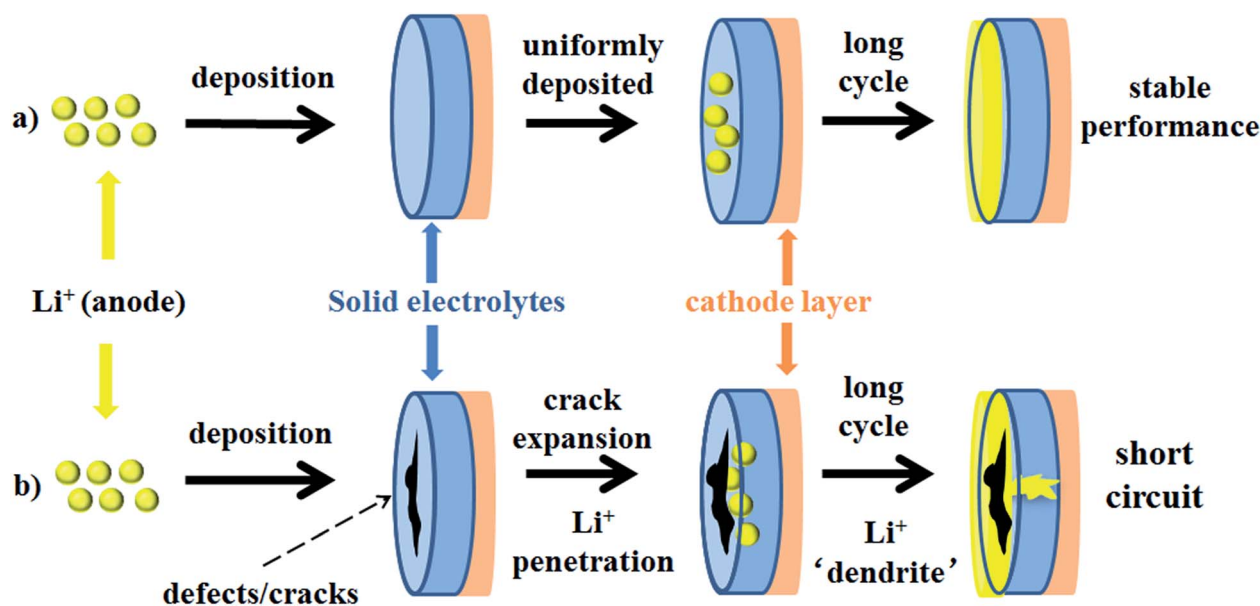This journal is © The Royal Society of Chemistry 2019

Fig. 22 Schematic diagrams of the mechanism of penetration of Li-ions into solid electrolytes. (a) Li-ions are uniformly deposited on the surface of the defect-free electrolyte; (b) penetration of Li-ions into the solid electrolyte layer forming 'dendrites' through defects, causing short circuit. Produced with permission. Copyright© 2017, John Wiley and Sons.

dendrites, it is necessary to prevent the interfacial reaction between the solid electrolyte and Li. Therefore, it is necessary to understand the mechanical parameters of sulfide solid electrolytes to analyse interface problems. The Young's modulus, hardness, and fracture toughness of glassy $70Li_2S–30P_2S_5$ solid electrolytes were determined to be 18.5 ± 0.9 GPa, 1.9 ± 0.2 GPa, and 0.23 ± 0.04 MPa $m^{1/2}$, respectively.[166] As illustrated in Fig. 20, $L_2S–P_2S_5$-type electrolytes are more compliant and brittle than crystalline oxide electrolytes. The low stiffness of the glassy electrolytes indicates that the electrolytes can accommodate mismatch in interfacial stress in all-solid-state batteries. But their ability is easily affected by low fracture toughness and cycling-generated flaws.

Monroe and Newman propose that solid electrolytes with sufficiently high shear modulus (about twice that of Li, which has shear modulus of 4.2 GPa)[167] could suppress the formation of Li dendrites.[168,169] However, this theory cannot explain the phenomenon that appeared in Porz et al.'s work.[165] There is still a disturbance by metal lithium dendrite growth in glassy $Li_2S–P_2S_5$ with a shear modulus of 8.3 GPa. The growth mechanism of lithium dendrites in four types of solid electrolytes, glassy $Li_2S–P_2S_5$, β-Li_3PS_4, and polycrystalline and single crystal LLZTO, is studied by galvanostatic electrodeposition experiments combined with *in situ* and *ex situ* microscopy. As shown in Fig. 21a, a model is proposed to explain the effect of stress accumulation on lithium dendrite growth. An electrochemomechanical model for growth of lithium-filled cracks is developed. Fig. 21b shows the relationship between the minimum over-potential and the defect size for glassy $Li_2S–P_2S_5$ and LLZTO. The relationship between maximum stress and defect size is also plotted. When studying the mechanism of lithium metal penetration through glassy $Li_2S–P_2S_5$, lithium

metal is uniformly deposited in the region of the glassy $Li_2S–P_2S_5$ with no crack and gradually propagates laterally from the electrode contact point as shown in Fig. 22a. However, when lithium metal is deposited near the precracked area, cracks are formed and extended into the sample, causing structural damage and even short-circuit as the experiment progressed, as in Fig. 22b. It is concluded that stabilization of the interfaces between solid electrolytes and lithium metal will require minimizing interface defects. The factors governing lithium penetration through brittle electrolytes are investigated by performing lithium electrodeposition on single-crystal $Li_6La_3ZrTaO_{12}$ garnets.[170] It is concluded that the risk of lithium metal penetration can be reduced by designing the battery with a larger cathode, smaller anode and small thickness/width ratio.

6 Conclusions and prospects

All-solid-state batteries are the most promising energy storage system for next generation applications, due to their good safety, high energy density and wide operating temperature. Among all the solid electrolytes, S-SEs have received extensive attention owing to their high conductivity, wide electrochemical window, and good mechanical properties. However, there are still great challenges for the application of S-SEs in all-solid-state batteries: (1) S-SEs are extremely sensitive to moisture and easily react with water in the air to produce toxic H_2S gas and therefore destroy the structure of the electrolyte; (2) problems of the interface between electrode/electrolyte still need to be settled.

This work mainly reviews the research progress of S-SEs and their applications in all-solid-state lithium and all-solid-state

Li–S batteries. The future development of emerging all-solid-state batteries should focus on the following aspects: (1) exploring new types of S-SEs or new preparation methods to improve the conductivity of Li-ions to meet practical applications; (2) enhancing the chemical and thermal stabilities of sulfide electrolytes; (3) improving the interface between the solid electrolytes and the electrodes; (4) optimizing the preparation process of all-solid-state batteries.

As the most promising energy storage system, there is still a long way to go in realizing the commercialization of all-solid-state batteries based on the requirements of safety, energy density and cycle stability.

Conflicts of interest

There are no conflicts to declare.

Acknowledgements

Notes and references

1 J. B. Goodenough and K. S. Park, *J. Am. Chem. Soc.*, 2013, **135**, 1167–1176.
2 L. Fan, H. L. Zhuang, L. Gao, Y. Lu and L. A. Archer, *J. Mater. Chem. A*, 2017, **5**, 3483–3492.
3 Q. Zhang, G. Peng, J. P. Mwizerwa, H. Wan, L. Cai, X. Xu and X. Yao, *J. Mater. Chem. A*, 2018, **6**, 12098–12105.
4 J. B. Goodenough, *J. Solid State Electrochem.*, 2012, **16**, 2019–2029.
5 K. Xu, *Chem. Rev.*, 2014, **114**, 11503–11618.
6 Z. Stoeva, I. Martin-Litas, E. Staunton, Y. G. Andreev and P. G. Bruce, *J. Am. Chem. Soc.*, 2003, **125**, 4619–4626.
7 Q. Pan, D. M. Smith, H. Qi, S. Wang and C. Y. Li, *Adv. Mater.*, 2015, **27**, 5995–6001.
8 C. Yuan, J. Li, P. Han, Y. Lai, Z. Zhang and J. Liu, *J. Power Sources*, 2013, **240**, 653–658.
9 R. Jalem, M. Nakayama and T. Kasuga, *Solid State Ionics*, 2014, **262**, 589–592.
10 Y. Harada, T. Ishigaki, H. Kawai and J. Kuwano, *Solid State Ionics*, 1998, **108**, 407–413.
11 H. Xu, S. Wang, H. Wilson, F. Zhao and A. Manthiram, *Chem. Mater.*, 2017, **29**, 7206–7212.
12 R. Murugan, V. Thangadurai and W. Weppner, *Angew. Chem., Int. Ed.*, 2007, **46**, 7778–7781.
13 V. Thangadurai and W. Weppner, *Ionics*, 2006, **12**, 81–92.
14 J. L. Fourquet, H. Duroy and M. P. Crosnier-Lopez, *J. Solid State Chem.*, 1996, **127**, 283–294.
15 Y. Wang, W. D. Richards, S. P. Ong, L. J. Miara, J. C. Kim, Y. Mo and G. Ceder, *Nat. Mater.*, 2015, **14**, 1026–1032.
16 A. Mei, X. Wang, Y. Feng, S. Zhao, G. Li, H. Geng, Y. Lin and C. Nan, *Solid State Ionics*, 2008, **179**, 2255–2259.

17 A. Hayashi, K. Noi, A. Sakuda and M. Tatsumisago, *Nat. Commun.*, 2012, **3**, 856–860.
18 A. Hayashi, A. Sakuda and M. Tatsumisago, *Front. Energy Res.*, 2016, **4**, 1–13.
19 J. H. Kennedy and Y. Yang, *J. Electrochem. Soc.*, 1986, **133**, 2437–24378.
20 C. Cao, Z.-B. Li, X.-L. Wang, X.-B. Zhao and W.-Q. Han, *Front. Energy Res.*, 2014, **2**, 1–10.
21 Y. Seino, T. Ota, K. Takada, A. Hayashi and M. Tatsumisago, *Energy Environ. Sci.*, 2014, **7**, 627–631.
22 Z. Liu, Y. Tang, X. Lü, G. Ren and F. Huang, *Ceram. Int.*, 2014, **40**, 15497–15501.
23 Y. Seino, K. Takada, B.-C. Kim, L. Zhang, N. Ohta, H. Wada, M. Osada and T. Sasaki, *Solid State Ionics*, 2005, **176**, 2389–2393.
24 T. Inada, K. Takada, A. Kajiyama, M. Kouguchi, H. Sasaki, S. Kondo, M. Watanabe, M. Murayama and R. Kanno, *Solid State Ionics*, 2003, **158**, 275–280.
25 M. Eom, S. Choi, S. Son, L. Choi, C. Park and D. Shin, *J. Power Sources*, 2016, **331**, 26–31.
26 H. Yamane, M. Shibata, Y. Shimane, T. Junke, Y. Seino, S. Adams, K. Minami, A. Hayashi and M. Tatsumisago, *Solid State Ionics*, 2007, **178**, 1163–1167.
27 B. Huang, X. Yao, Z. Huang, Y. Guan, Y. Jin and X. Xu, *J. Power Sources*, 2015, **284**, 206–211.
28 M. Kotobuki and M. Koishi, *Ceram. Int.*, 2013, **39**, 4645–4649.
29 M. Tatsumisago, M. Nagao and A. Hayashi, *J. Asian Ceram. Soc.*, 2018, **1**, 17–25.
30 R. Kanno and M. Murayama, *J. Electrochem. Soc.*, 2001, **148**, A742–A746.
31 M. Ribes, B. Barrau and J. Souquet, *J. Non-Cryst. Solids*, 1980, **38**, 271–276.
32 R. Mercier, J.-P. Malugani, B. Fahys and G. Robert, *Solid State Ionics*, 1981, **5**, 663–666.
33 A. Hayashi, S. Hama, T. Minami and M. Tatsumisago, *Electrochem. Commun.*, 2003, **5**, 111–114.
34 Z. Liu, W. Fu, E. A. Payzant, X. Yu, Z. Wu, N. J. Dudney, J. Kiggans, K. Hong, A. J. Rondinone and C. Liang, *J. Am. Chem. Soc.*, 2013, **135**, 975–978.
35 Y. Zhang, R. Chen, T. Liu, Y. Shen, Y. Lin and C. W. Nan, *ACS Appl. Mater. Interfaces*, 2017, **9**, 28542–28548.
36 Y. Inoue, K. Suzuki, N. Matsui, M. Hirayama and R. Kanno, *J. Solid State Chem.*, 2017, **246**, 334–340.
37 Y. Kato, S. Hori, T. Saito, K. Suzuki, M. Hirayama, A. Mitsui, M. Yonemura, H. Iba and R. Kanno, *Nat. Energy*, 2016, **1**, 1–7.
38 N. Kamaya, K. Homma, Y. Yamakawa, M. Hirayama, R. Kanno, M. Yonemura, T. Kamiyama, Y. Kato, S. Hama, K. Kawamoto and A. Mitsui, *Nat. Mater.*, 2011, **10**, 682–686.
39 P. Bron, S. Johansson, K. Zick, J. Schmedt auf der Gunne, S. Dehnen and B. Roling, *J. Am. Chem. Soc.*, 2013, **135**, 15694–15697.
40 J. M. Whiteley, J. H. Woo, E. Hu, K.-W. Nam and S.-H. Lee, *J. Electrochem. Soc.*, 2014, **161**, A1812–A1817.
41 P. Zhou, J. Wang, F. Cheng, F. Li and J. Chen, *Chem. Commun.*, 2016, **52**, 6091–6094.

42 S. Boulineau, M. Courty, J.-M. Tarascon and V. Viallet, *Solid State Ionics*, 2012, **221**, 1–5.

43 V. Epp, Ö. Gün, H.-J. Deiseroth and M. Wilkening, *J. Phys. Chem. Lett.*, 2013, **4**, 2118–2123.

44 A. Hayashi, H. Yamashita, M. Tatsumisago and T. Minami, *Solid State Ionics*, 2002, **148**, 381–389.

45 J. P. Malugani, R. Mercier and M. Tachez, *Solid State Ionics*, 1986, **21**, 131–138.

46 H. Muramatsu, A. Hayashi, T. Ohtomo, S. Hama and M. Tatsumisago, *Solid State Ionics*, 2011, **182**, 116–119.

47 K. Homma, M. Yonemura, T. Kobayashi, M. Nagao, M. Hirayama and R. Kanno, *Solid State Ionics*, 2011, **182**, 53–58.

48 N. H. H. Phuc, K. Morikawa, T. Mitsuhiro, H. Muto and A. Matsuda, *Ionics*, 2017, **23**, 2061–2067.

49 K. Minami, A. Hayashi and M. Tatsumisago, *J. Am. Ceram. Soc.*, 2011, **94**, 1779–1783.

50 F. Mizuno, A. Hayashi, K. Tadanaga and M. Tatsumisago, *Adv. Mater.*, 2005, **17**, 918–921.

51 F. Mizuno, A. Hayashi, K. Tadanaga and M. Tatsumisago, *Solid State Ionics*, 2006, **177**, 2721–2725.

52 Y. Wang, D. Lu, M. Bowden, P. Z. El Khoury, K. S. Han, Z. D. Deng, J. Xiao, J.-G. Zhang and J. Liu, *Chem. Mater.*, 2018, **30**, 990–997.

53 T. Ohtomo, A. Hayashi, M. Tatsumisago and K. Kawamoto, *J. Solid State Electrochem.*, 2013, **17**, 2551–2557.

54 Y. Mo, S. P. Ong and G. Ceder, *Chem. Mater.*, 2011, **24**, 15–17.

55 S. P. Ong, Y. Mo, W. D. Richards, L. Miara, H. S. Lee and G. Ceder, *Energy Environ. Sci.*, 2013, **6**, 148–156.

56 A. Kuhn, O. Gerbig, C. Zhu, F. Falkenberg, J. Maier and B. V. Lotsch, *Phys. Chem. Chem. Phys.*, 2014, **16**, 14669–14674.

57 W. F. Kuhs, R. Nitsch and K. Scheunemann, *Acta Crystallogr., Sect. B: Struct. Crystallogr. Cryst. Chem.*, 1978, **34**, 64–70.

58 S. Geller, *Z. Kristallogr.*, 1979, **149**, 31.

59 B. Krebs and J. Mandt, *Z. Naturforsch., B: Anorg. Chem., Org. Chem.*, 1977, **32**, 373.

60 W. F. Kuhs, R. Nitsch and K. Scheunemann, *Mater. Res. Bull.*, 1979, **14**, 241–248.

61 E. E. Hellstrom and R. A. Huggins, *J. Solid State Chem.*, 1980, **35**, 207–214.

62 F. Boucher, M. Evain and R. Brec, *J. Solid State Chem.*, 1993, **107**, 332–346.

63 H. Wada, M. Ishii, M. Onoda, M. Tansho and A. Sato, *Solid State Ionics*, 1996, **86**, 159–163.

64 M. Evain, E. Gaudin, F. Boucher, V. Petricek and F. Taulelle, *Acta Crystallogr., Sect. B: Struct. Sci.*, 1998, **54**, 376–383.

65 E. Gaudin, F. Boucher, V. Petricek, F. Taulelle and M. Evain, *Acta Crystallogr., Sect. B: Struct. Sci.*, 2000, **56**, 402–408.

66 R. Belin, L. Aldon, A. Zerouale, C. Belin and M. Ribes, *Solid State Sci.*, 2001, **3**, 251–265.

67 E. Gaudin, H. J. Deiseroth and T. Zaiß, *Z. Kristallogr.*, 2001, **216**, 39–44.

68 H.-J. Deiseroth, J. Maier, K. Weichert, V. Nickel, S.-T. Kong and C. Reiner, *Z. Anorg. Allg. Chem.*, 2011, **637**, 1287–1294.

69 N. J. J. de Klerk, I. Rosłoń and M. Wagemaker, *Chem. Mater.*, 2016, **28**, 7955–7963.

70 H. M. Chen, C. Maohua and S. Adams, *Phys. Chem. Chem. Phys.*, 2015, **17**, 16494–16506.

71 H. J. Deiseroth, S. T. Kong, H. Eckert, J. Vannahme, C. Reiner, T. Zaiss and M. Schlosser, *Angew. Chem., Int. Ed.*, 2008, **47**, 755–758.

72 M. A. Kraft, S. P. Culver, M. Calderon, F. Bocher, T. Krauskopf, A. Senyshyn, C. Dietrich, A. Zevalkink, J. Janek and W. G. Zeier, *J. Am. Chem. Soc.*, 2017, **139**, 10909–10918.

73 R. P. Rao and S. Adams, *Phys. Status Solidi A*, 2011, **208**, 1804–1807.

74 R. R. Prasada, N. Sharma, V. K. Peterson and S. Adams, *Solid State Ionics*, 2013, **230**, 72–76.

75 P. R. Rayavarapu, N. Sharma, V. K. Peterson and S. Adams, *J. Solid State Chem.*, 2011, **16**, 1807–1813.

76 M. Chen, R. P. Rao and S. Adams, *Solid State Ionics*, 2014, **262**, 183–187.

77 M. Chen and S. Adams, *J. Solid State Electrochem.*, 2014, **19**, 697–702.

78 M. Chen, R. Prasada Rao and S. Adams, *Solid State Ionics*, 2014, **268**, 300–304.

79 M. Chen, X. Yin, M. V. Reddy and S. Adams, *J. Mater. Chem. A*, 2015, **3**, 10698–10702.

80 Z. Zhang, L. Zhang, Y. Liu, C. Yu, X. Yan, B. Xu and L.-m. Wang, *J. Alloys Compd.*, 2018, **747**, 227–235.

81 Z. Zhang, Y. Shao, B. Lotsch, Y.-S. Hu, H. Li, J. r. Janek, L. F. Nazar, C.-W. Nan, J. Maier, M. Armand and L. Chen, *Energy Environ. Sci.*, 2018, **11**, 1945–1976.

82 B. D. McCloskey, *J. Phys. Chem. Lett.*, 2015, **6**, 4581–4588.

83 Y. Kato, K. Kawamoto, R. Kanno and M. Hirayama, *Electrochemistry*, 2012, **80**, 749–751.

84 Z. Zhang, Y. Shao, B. Lotsch, Y. S. Hu, H. Li, J. Janek, L. F. Nazar, C. W. Nan, J. Maier, M. Armand and L. Chen, *Energy Environ. Sci.*, 2018, **11**, 1945–1976.

85 X. Judez, G. G. Eshetu, C. Li, L. M. Rodriguez-Martinez, H. Zhang and M. Armand, *Joule*, 2018, **2**, 2208–2224.

86 A. Manthiram, X. Yu and S. Wang, *Nat. Rev. Mater.*, 2017, **2**, 16103.

87 J. Haruyama, K. Sodeyama, L. Han, K. Takada and Y. Tateyama, *Chem. Mater.*, 2014, **26**, 4248–4255.

88 J. W. Fergus, *J. Power Sources*, 2010, **195**, 4554–4569.

89 D. Aurbach, *J. Electrochem. Soc.*, 1996, **143**, 3525.

90 W. Xu, J. Wang, F. Ding, X. Chen, E. Nasybulin, Y. Zhang and J.-G. Zhang, *Energy Environ. Sci.*, 2014, **7**, 513–537.

91 N. Ohta, K. Takada, L. Zhang, R. Ma, M. Osada and T. Sasaki, *Adv. Mater.*, 2006, **18**, 2226–2229.

92 W. Zhang, D. A. Weber, H. Weigand, T. Arlt, I. Manke, D. Schroder, R. Koerver, T. Leichtweiss, P. Hartmann, W. G. Zeier and J. Janek, *ACS Appl. Mater. Interfaces*, 2017, **9**, 17835–17845.

93 Y. Tian, T. Shi, W. D. Richards, J. Li, J. C. Kim, S.-H. Bo and G. Ceder, *Energy Environ. Sci.*, 2017, **10**, 1150–1166.

94 B. Wu, S. Wang, W. J. Evans IV, D. Z. Deng, J. Yang and J. Xiao, *J. Mater. Chem. A*, 2016, **4**, 15266–15280.

95 N. J. J. de Klerk and M. Wagemaker, *ACS Appl. Energy Mater.*, 2018, **1**, 5609–5618.

96 L. Xu, S. Tang, Y. Cheng, K. Wang, J. Liang, C. Liu, Y.-C. Cao, F. Wei and L. Mai, *Joule*, 2018, **2**, 1991–2015.

97 A. C. Luntz, J. Voss and K. Reuter, *J. Phys. Chem. Lett.*, 2015, **6**, 4599–4604.

98 N. Ohta, K. Takada, L. Zhang, R. Ma, M. Osada and T. Sasaki, *Adv. Mater.*, 2006, **18**, 2226–2229.

99 A. Sakuda, A. Hayashi and M. Tatsumisago, *Chem. Mater.*, 2010, **22**, 949–956.

100 J. Maier, *Nat. Mater.*, 2005, **4**, 805–815.

101 J. Maier, *Solid State Chem.*, 1995, **23**, 171–263.

102 N. Ohta, K. Takada, I. Sakaguchi, L. Zhang, R. Ma, K. Fukuda, M. Osada and T. Sasaki, *Electrochem. Commun.*, 2007, **9**, 1486–1490.

103 K. Ozawa, *Solid State Ionics*, 1994, **69**, 212–221.

104 R. Koksbang, J. Barker, H. Shi and M. Y. Sadi, *Solid State Ionics*, 1996, **84**, 1–21.

105 K. Mizushima, P. C. Jones, P. J. Wiseman and J. B. Goodenough, *Mater. Res. Bull.*, 1980, **15**, 783–789.

106 K. Takada, N. Ohta, L. Zhang, X. Xu, B. T. Hang, T. Ohnishi, M. Osada and T. Sasaki, *Solid State Ionics*, 2012, **225**, 594–597.

107 X. Xu, K. Takada, K. Fukuda, T. Ohnishi, K. Akatsuka, M. Osada, B. T. Hang, K. Kumagai, T. Sekiguchi and T. Sasaki, *Energy Environ. Sci.*, 2011, **4**, 3509.

108 A. Sakuda, H. Kitaura, A. Hayashi, K. Tadanaga and M. Tatsumisago, *J. Electrochem. Soc.*, 2009, **156**, A27.

109 Y. Ito, S. Yamakawa, A. Hayashi and M. Tatsumisago, *J. Mater. Chem. A*, 2017, **5**, 10658–10668.

110 D. K. Kim, P. Muralidharan, H.-W. Lee, R. Ruffo, Y. Yang, C. K. Chan, H. Peng, R. A. Huggins and Y. Cui, *Nano Lett.*, 2008, **8**, 3948–3952.

111 E. Hosono, T. Kudo, I. Honma, H. Matsuda and H. Zhou, *Nano Lett.*, 2009, **9**, 1045–1051.

112 H. W. Lee, P. Muralidharan, R. Ruffo, C. M. Mari, Y. Cui and D. K. Kim, *Nano Lett.*, 2010, **10**, 3852–3856.

113 H. Kitaura, A. Hayashi, K. Tadanaga and M. Tatsumisago, *Solid State Ionics*, 2011, **192**, 304–307.

114 S. Yubuchi, Y. Ito, T. Matsuyama, A. Hayashi and M. Tatsumisago, *Solid State Ionics*, 2016, **285**, 79–82.

115 G. Oh, M. Hirayama, O. Kwon, K. Suzuki and R. Kanno, *Chem. Mater.*, 2016, **28**, 2634–2640.

116 R. Koerver, I. Aygün, T. Leichtweiß, C. Dietrich, W. Zhang, J. O. Binder, P. Hartmann, W. G. Zeier and J. Janek, *Chem. Mater.*, 2017, **29**, 5574–5582.

117 Y.-K. Sun, S.-T. Myung, B.-C. Park, J. Prakash, I. Belharouak and K. Amine, *Nat. Mater.*, 2009, **8**, 320–324.

118 Y.-K. Sun, Z. Chen, H.-J. Noh, D.-J. Lee, H.-G. Jung, Y. Ren, S. Wang, C. S. Yoon, S.-T. Myung and K. Amine, *Nat. Mater.*, 2012, **11**, 942–947.

119 Y.-Y. Wang, Y.-Y. Sun, S. Liu, G.-R. Li and X.-P. Gao, *ACS Appl. Energy Mater.*, 2018, **1**, 3881–3889.

120 N. Machida, J. Kashiwagi, M. Naito and T. Shigematsu, *Solid State Ionics*, 2012, **225**, 354–358.

121 S. Ito, S. Fujiki, T. Yamada, Y. Aihara, Y. Park, T. Y. Kim, S.-W. Baek, J.-M. Lee, S. Doo and N. Machida, *J. Power Sources*, 2014, **248**, 943–950.

122 Y. Seino, T. Ota and K. Takada, *J. Power Sources*, 2011, **196**, 6488–6492.

123 G. Peng, X. Yao, H. Wan, B. Huang, J. Yin, F. Ding and X. Xu, *J. Power Sources*, 2016, **307**, 724–730.

124 X. Xu, K. Takada, K. Watanabe, I. Sakaguchi, K. Akatsuka, B. T. Hang, T. Ohnishi and T. Sasaki, *Chem. Mater.*, 2011, **23**, 3798–3804.

125 S. Takai, M. Kamata, S. Fujine, K. Yoneda, K. Kanda and T. Esaka, *Solid State Ionics*, 1999, **123**, 165–172.

126 Y. Deng, C. Eames, J.-N. Chotard, F. Lalère, V. Seznec, S. Emge, O. Pecher, C. P. Grey, C. Masquelier and M. S. Islam, *J. Am. Chem. Soc.*, 2015, **137**, 9136–9145.

127 B. Zhang, X. Qin, G. R. Li and X. P. Gao, *Energy Environ. Sci.*, 2010, **3**, 1531.

128 R. D. Rauh, K. M. Abraham, G. F. Pearson, J. K. Surprenant and S. B. Brummer, *J. Electrochem. Soc.*, 1979, **126**, 523–527.

129 D. R. Rolison and L. F. Nazar, *MRS Bull.*, 2011, **36**, 486–493.

130 Y. Yang, G. Zheng, S. Misra, J. Nelson, M. F. Toney and Y. Cui, *J. Am. Chem. Soc.*, 2012, **134**, 15387–15394.

131 N. S. Choi, Z. Chen, S. A. Freunberger, X. Ji, Y. K. Sun, K. Amine, G. Yushin, L. F. Nazar, J. Cho and P. G. Bruce, *Angew. Chem., Int. Ed.*, 2012, **51**, 9994–10024.

132 A. Manthiram, Y. Fu and Y. Su, *Acc. Chem. Res.*, 2013, **46**, 1125–1134.

133 X.-P. Gao and H.-X. Yang, *Energy Environ. Sci.*, 2010, **3**, 174–189.

134 M. Wild, L. O'Neill, T. Zhang, R. Purkayastha, G. Minton, M. Marinescu and G. J. Offer, *Energy Environ. Sci.*, 2015, **8**, 3477–3494.

135 S. Evers and L. F. Nazar, *Acc. Chem. Res.*, 2013, **46**, 1135–1143.

136 A. Manthiram, Y. Fu, S. H. Chung, C. Zu and Y. S. Su, *Chem. Rev.*, 2014, **114**, 11751–11787.

137 Y. Yang, G. Zheng and Y. Cui, *Chem. Soc. Rev.*, 2013, **42**, 3018–3032.

138 M. Nagao, A. Hayashi and M. Tatsumisago, *J. Mater. Chem.*, 2012, **22**, 10015.

139 A. Hayashi, T. Ohtomo, F. Mizuno, K. Tadanaga and M. Tatsumisago, *Electrochem. Commun.*, 2003, **5**, 701–705.

140 T. Takeuchi, H. Kageyama, K. Nakanishi, M. Tabuchi, H. Sakaebe, T. Ohta, H. Senoh, T. Sakai and K. Tatsumi, *J. Electrochem. Soc.*, 2010, **157**, A1196.

141 K. Suzuki, D. Kato, K. Hara, T.-a. Yano, M. Hirayama, M. Hara and R. Kanno, *Electrochim. Acta*, 2017, **258**, 110–115.

142 N. Tanibata, H. Tsukasaki, M. Deguchi, S. Mori, A. Hayashi and M. Tatsumisago, *J. Mater. Chem. A*, 2017, **5**, 11224–11228.

143 H. Nagata and Y. Chikusa, *Chem. Lett.*, 2014, **43**, 1335–1336.

144 S. Kinoshita, K. Okuda, N. Machida, M. Naito and T. Sigematsu, *Solid State Ionics*, 2014, **256**, 97–102.

145 M. Nagao, A. Hayashi and M. Tatsumisago, *Electrochim. Acta*, 2011, **56**, 6055–6059.

146 M. Nagao, A. Hayashi and M. Tatsumisago, *Energy Technol.*, 2013, **1**, 186–192.

147 H. Nagata and Y. Chikusa, *J. Power Sources*, 2014, **264**, 206–210.

148 J. E. Trevey, J. R. Gilsdorf, C. R. Stoldt, S.-H. Lee and P. Liu, *J. Electrochem. Soc.*, 2012, **159**, A1019–A1022.

149 Y. Yang, M. T. McDowell, A. Jackson, J. J. Cha, S. S. Hong and Y. Cui, *Nano Lett.*, 2010, **10**, 1486–1491.

150 C. Nan, Z. Lin, H. Liao, M. K. Song, Y. Li and E. J. Cairns, *J. Am. Chem. Soc.*, 2014, **136**, 4659–4663.

151 Z. Lin, Z. Liu, N. J. Dudney and C. Liang, *ACS Nano*, 2013, **7**, 2829–2833.

152 P. Long, Q. Xu, G. Peng, X. Yao and X. Xu, *ChemElectroChem*, 2016, **3**, 764–769.

153 D. Y. Oh, Y. E. Choi, D. H. Kim, Y.-G. Lee, B.-S. Kim, J. Park, H. Sohn and Y. S. Jung, *J. Mater. Chem. A*, 2016, **4**, 10329–10335.

154 Q. Zhang, X. Yao, J. P. Mwizerwa, N. Huang, H. Wan, Z. Huang and X. Xu, *Solid State Ionics*, 2018, **318**, 60–64.

155 Q. Zhang, J. P. Mwizerwa, H. Wan, L. Cai, X. Xu and X. Yao, *J. Mater. Chem. A*, 2017, **5**, 23919–23925.

156 J. B. Goodenough and Y. Kim, *Chem. Mater.*, 2010, **22**, 587–603.

157 M. Nagao, A. Hayashi, M. Tatsumisago, T. Kanetsuku, T. Tsuda and S. Kuwabata, *Phys. Chem. Chem. Phys.*, 2013, **15**, 18600–18606.

158 R. Xu, S. Zhang, X. Wang, Y. Xia, X. Xia, J. Wu, C. Gu and J. Tu, *Chemistry*, 2018, **24**, 6007–6018.

159 S. Wenzel, S. Randau, T. Leichtweiß, D. A. Weber, J. Sann, W. G. Zeier and J. Janek, *Chem. Mater.*, 2016, **28**, 2400–2407.

160 K. Takada, N. Aotani, K. Iwamoto and S. Kondo, *Solid State Ionics*, 1996, **86**, 877–882.

161 H. Kitaura, A. Hayashi, K. Tadanaga and M. Tatsumisago, *J. Electrochem. Soc.*, 2009, **156**, A114.

162 E. Rangasamy, Z. Liu, M. Gobet, K. Pilar, G. Sahu, W. Zhou, H. Wu, S. Greenbaum and C. Liang, *J. Am. Chem. Soc.*, 2015, **137**, 1384–1387.

163 M. Ogawa, R. Kanda, K. Yoshida, T. Uemura and K. Harada, *J. Power Sources*, 2012, **205**, 487–490.

164 R. Xu, F. Han, X. Ji, X. Fan, J. Tu and C. Wang, *Nano Energy*, 2018, **53**, 958–966.

165 L. Porz, T. Swamy, B. W. Sheldon, D. Rettenwander, T. Frömling, H. L. Thaman, S. Berendts, R. Uecker, W. C. Carter and Y.-M. Chiang, *Adv. Energy Mater.*, 2017, **7**, 1701003.

166 F. P. McGrogan, T. Swamy, S. R. Bishop, E. Eggleton, L. Porz, X. Chen, Y.-M. Chiang and K. J. Van Vliet, *Adv. Energy Mater.*, 2017, **7**, 1602011.

167 A. Sharafi, H. M. Meyer, J. Nanda, J. Wolfenstine and J. Sakamoto, *J. Power Sources*, 2016, **302**, 135–139.

168 C. Monroe and J. Newman, *J. Electrochem. Soc.*, 2004, **151**, A880.

169 C. Monroe and J. Newman, *J. Electrochem. Soc.*, 2005, **152**, A396.

170 T. Swamy, R. Park, B. W. Sheldon, D. Rettenwander, L. Porz, S. Berendts, R. Uecker, W. C. Carter and Y.-M. Chiang, *J. Electrochem. Soc.*, 2018, **165**, A3648–A3655.

This journal is © The Royal Society of Chemistry 2019

J. Mater. Chem. A, 2019, **7**, 20540–20557 | **20557**